PHILOSOPHICAL TRANSACTIONS OF THE ROYAL SOCIETY A

rsta.royalsocietypublishing.org

Research

Cite this article: Herrera-Valencia EE, Rey AD. 2014 Actuation of flexoelectric membranes in viscoelastic fluids with applications to outer hair cells. *Phil. Trans. R. Soc. A* **372**: 20130369. http://dx.doi.org/10.1098/rsta.2013.0369

One contribution of 10 to a Theme Issue 'New trends in active liquid crystals: mechanics, dynamics and applications'.

Subject Areas:
biophysics, fluid mechanics, mechanics, chemical engineering, materials science, biomechanics

Keywords:
flexoelectric membrane actuation, flexoelectric-driven viscoelastic capillary flow, rheological transfer function in outer hair cells

Author for correspondence:
Alejandro D. Rey
e-mail: alejandro.rey@mcgill.ca

Royal Society Publishing

Actuation of flexoelectric membranes in viscoelastic fluids with applications to outer hair cells

E. E. Herrera-Valencia[1] and Alejandro D. Rey[2]

[1]Chemical Engineering Department, Faculty of Higher Education Zaragoza. National Autonomous University of Mexico. Campus I: Av Guelatao No. 66 Col. Ejército de Oriente, Iztapalapa, C.P. 09230, México

[2]Department of Chemical Engineering, McGill University, 3610 University Street, Montreal, Quebec, Canada H3A 2B2

Liquid crystal flexoelectric actuation uses an imposed electric field to create membrane bending, and it is used by the outer hair cells (OHCs) located in the inner ear, whose role is to amplify sound through generation of mechanical power. Oscillations in the OHC membranes create periodic viscoelastic flows in the contacting fluid media. A key objective of this work on flexoelectric actuation relevant to OHCs is to find the relations and impact of the electromechanical properties of the membrane, the rheological properties of the viscoelastic media, and the frequency response of the generated mechanical power output. The model developed and used in this work is based on the integration of: (i) the flexoelectric membrane shape equation applied to a circular membrane attached to the inner surface of a circular capillary and (ii) the coupled capillary flow of contacting viscoelastic phases, such that the membrane flexoelectric oscillations drive periodic viscoelastic capillary flows, as in OHCs. By applying the Fourier transform formalism to the governing equation, analytical expressions for the transfer function associated with the curvature and electrical field and for the power dissipation of elastic storage energy were found.

1. Introduction

In nature and physiology, biological liquid crystals (LCs) play significant roles as multifunctional materials [1]. This paper presents theory and simulation of a

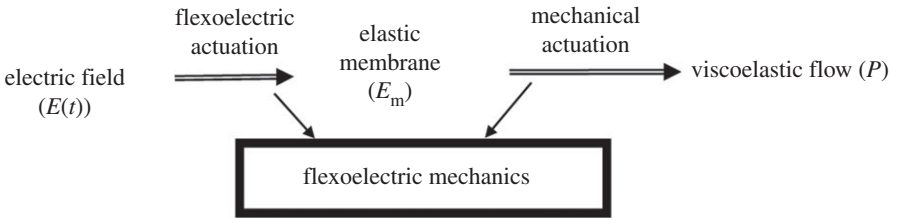

Figure 1. Schematic of the processes and mechanisms currently accepted to be involved in the functioning of OHCs. The oscillating electric field $E(t)$ distorts the membrane through the flexoelectric effect. The membrane elastic E_m curvature distortions are transferred to contacting viscoelastic fluids and deliver mechanical power P. The combination of flexoelectric actuation and mechanical actuation is flexoelectric mechanics (adapted from [11]).

physiological actuator device whose functioning hinges on unique electromechanical properties of mesophases and that provides an example of responsive self-organized materials. The functioning of outer hair cells (OHCs) in the inner ear involves electric field-driven periodic curvature oscillations of LC elastic membranes that impart momentum and flow to the contacting viscoelastic fluids; the electric field actuation of the LC membrane is known as flexoelectricity [1–12]. The key role of OHCs is sound amplification in the presence of viscous dissipation and elastic storage [10]. Hence, the full description and understanding of OHC functioning has to include the frequency response of flexoelectric membranes embedded in viscous and viscoelastic media due to an oscillating **E** field [11–15]. The field of flexoelectric membranes was pioneered and developed by Petrov and co-workers [2–4,10].

The generic and key features of the electrical to mechanical energy conversion system in OHCs are described in figure 1 (figure 3 shows additional details). The input oscillating **E** field, through the electromechanical flexoelectric effect, produces curvature oscillations in the elastic membrane that forms the OHC [11–15] and that is surrounded by viscoelastic media. In turn, the oscillating elastic membrane displaces the contacting viscoelastic liquids through the mechanical viscoelasto-elasticity effect [11]. The combined effect that allows the electromechanical energy conversion is based on the integration of the flexoelectric effect (**E** field imposed on flexoelectric membrane) and the mechanical effect (membrane elasticity plus viscoelastic bulk fluid flow) [14,15]. The two key issues in this energy conversion device are

(i) how much power P is eventually delivered to the contacting viscoelastic fluids from the imposed oscillating electric field **E** and how much stored membrane elastic energy E_m is required to deliver that power and
(ii) under which material conditions is a well-localized resonant power peak found (in the spectrum of P), as physiologically required [11].

As expected, the issues (i) and (ii) identified above depend on (a) the **E**-frequency ω [11] as well as on (b) the material properties of the bio-device components discussed below.

(a) Frequency response

The intensity of the linear momentum transfer from the oscillating membrane to the contacting viscoelastic fluids depends on the imposed frequency [11]. Hence frequency-dependent viscoelasticity is an essential ingredient of this important biological LC electro-mechanical oscillator [11]. Viscoelasticity is an important frequency-dependent property of synthetic and biological materials and processes [16–19]. Biological systems respond differently to inputs of different frequencies [11]. Some systems may amplify components of certain frequencies, and attenuate components of other frequencies [19,20], and this property is crucial to understanding the processes that control the functioning of OHCs [20–25] and hearing processes [26–28]. The frequency response [29] is the relationship between the system input and

output in the Fourier domain:

$$I(jw)F_{\mathrm{D}}(jw) = O(jw), \tag{1.1}$$

where $I(jw)$ is the system input, $O(jw)$ the system output and $F_{\mathrm{D}}(jw)$ the frequency response. Since the frequency response $F_{\mathrm{D}}(jw)$ is a complex function, we can convert it to polar notation

$$F_{\mathrm{D}}(jw) = \mathrm{Re}[F_{\mathrm{D}}(jw)] + \mathrm{Im}[F_{\mathrm{D}}(jw)] = |F_{\mathrm{D}}(jw)|\exp(\phi j). \tag{1.2}$$

The magnitude $|F_D(jw)|$ represents the system's tendency to amplify or attenuate the input signal. For the OHC, we show below in detail (figure 3 and §§2–4) that the inputs are the periodic electric field $E(t)$ generated by the incoming acoustic waves, and the outputs are the volumetric flow rates of the contacting fluids and the membrane curvature. The phase angle ϕ in equation (1.2) is

$$\phi = \arctan \frac{\mathrm{Im}\{F_{\mathrm{D}}(jw)\}}{\mathrm{Re}\{F_{\mathrm{D}}(jw)\}}, \tag{1.3}$$

and it represents the tendency to delay the input signal and is intimately related to the memory of the fluids. Besides the role of fluid viscoelasticity, the functioning of OHCs is based on LC flexoelectricity [1–4]. Hence, a key to OHC modelling that we have performed in this paper is to determine and characterize $F_{\mathrm{D}}(jw)$ in terms of LC membrane flexoelectric elasticity and frequency-dependent fluid viscoelasticity. Then, we use these results to compute dissipation and elastic storage in our OHC model.

(b) Materials

Nematic liquid crystals are multifunctional self-organizing viscoelastic anisotropic materials whose orientational order responds to external flow, electromagnetic, chemical, optical and surface fields [11,17–19]; the orientational order is defined by the director $\mathbf{n}$ and the elastic distortions by director gradients $\nabla\mathbf{n}$ [11,17–19]. A distinguishing and novel property of nematics is flexoelectricity [1–4,11], which describes the coupling between orientational gradients and electric polarization, such that an applied electric field creates orientational distortions and distortions create macroscopic polarization [1–4,11,17–19]. The polar nature of splay $\mathbf{S} = \mathbf{n}\nabla\cdot\mathbf{n}$ and bend $\mathbf{B} = -\mathbf{n}\times\nabla\times\mathbf{n}$ orientational deformations can polarize the nematic LC medium [11–13]:

$$\mathbf{P}_{\mathrm{f}} = c_{\mathrm{S}}\mathbf{S} + c_{\mathrm{B}}\mathbf{B}, \tag{1.4}$$

where $\mathbf{P}_{\mathrm{f}}$ is the flexoelectric polarization, and where the flexoelectric coefficients for splay and bend $\{c_{\mathrm{S}}, c_{\mathrm{B}}\}$ are of the order of $10\,\mathrm{pC\,m^{-1}}$. Equation (1.4) describes a sensor or the direct flexoelectric effect [11–13] where the deformation creates polarization. The actuation or converse flexoelectric effect [11–13] describes the flexoelectric director torque $\boldsymbol{\Gamma}_{\mathrm{f}}$ due to an electric field $\mathbf{E}$

$$\boldsymbol{\Gamma}_{\mathrm{f}} = \mathbf{n}\times\{(c_{\mathrm{S}} - c_{\mathrm{B}})[\mathbf{E}\nabla\cdot\mathbf{n} - \nabla(\mathbf{n}\cdot\mathbf{E})] + (c_{\mathrm{S}} + c_{\mathrm{B}})\mathbf{n}\cdot\nabla\mathbf{E}\}, \tag{1.5}$$

where we note that $\boldsymbol{\Gamma}_{\mathrm{f}}$ depends on $\mathbf{E}$ and $\nabla\mathbf{E}$. The torque $\boldsymbol{\Gamma}_{\mathrm{f}}$ is given by the sum of a flexoelectric stress $\mathbf{T}_{\mathrm{f}}$ and flexoelectric couple stress $\mathbf{C}_{\mathrm{f}}$:

$$\boldsymbol{\Gamma}_{\mathrm{f}} = -\boldsymbol{\varepsilon} : \mathbf{T}_{\mathrm{f}} + \nabla\cdot\mathbf{C}_{\mathrm{f}} \tag{1.6}$$

indicating how an $\mathbf{E}$ field creates a mechanical effect. The current potential applications of LC flexoelectricity include energy harvesting, electromechanical transducers and displays [11,14,15]. The electro-elasticity of synthetic and biological membranes can be efficiently described by LC models, using an approach denoted by nemato-membranology [11–15]. For example, the elasticity of biological lipid bilayer membranes is well described by the well-known Helfrich energy E_{H} for

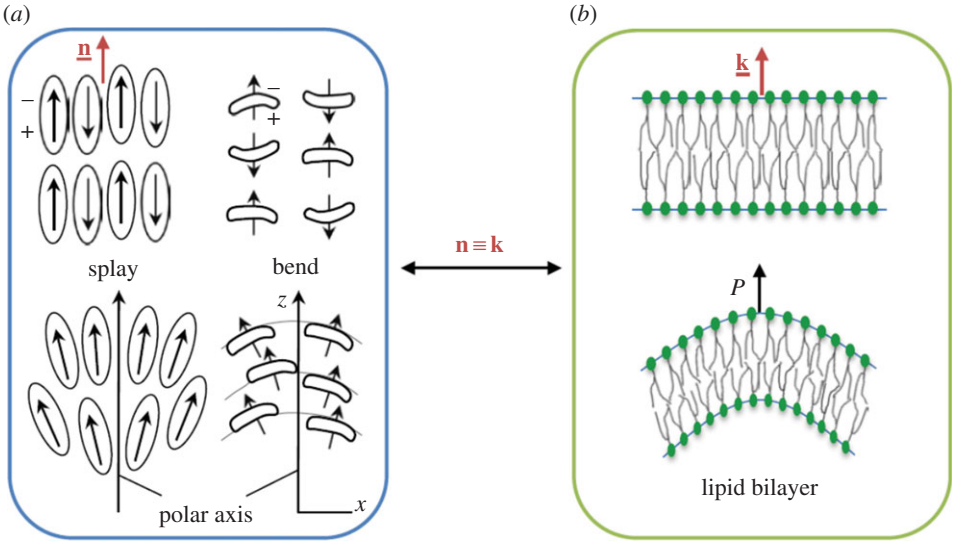

Figure 2. (*a*) Flexoelectricity in rod-like and banana-shaped nematic LCs due to slay and bend deformations of the director **n**. (*b*) Flexoelectricity in biological membranes due to bending curvature described by surface gradients of the unit normal **k**. The correspondence between nematic flexoelectricity and membrane flexoelectricity is obtained when the director **n** is identified with the membrane unit normal **k** (adapted from [11]). (Online version in colour.)

bending $2k_cH^2$ and torsion $\bar{k}_cK$:

$$E_H = 2k_cH^2 + \bar{k}_cK, \tag{1.7}$$

where H is the average curvature and K the Gaussian curvature, which follows from the nematic Frank elastic energy [11–15]:

$$E_F = \frac{K_1}{2}(\nabla \cdot \mathbf{n})^2 - K_{24}\nabla \cdot (\mathbf{n}\nabla \cdot \mathbf{n} + \mathbf{n} \times \nabla \times \mathbf{n}), \tag{1.8}$$

where K_1 is the splay and K_{24} is the saddle-splay constant; the geometrical quantities and definitions used in this paper are reported elsewhere [11,17–19]. Nemato-membranology is applied by identifying the director **n** with the outer unit normal $\mathbf{n} = \mathbf{k}$ in equation (1.8), and considering surface gradient ∇_s, we obtain

$$E_F = \left(\frac{K_1}{2} + 4K_{24}\right)H^2 + (-2K_{24})\,K, \tag{1.9}$$

which coincides with E_H, and gives $4k_c = (K_1 + 8K_{24}), \bar{k}_c = -2K_{24}$; the surface gradient is given by the tangential projection of the total gradient: $\nabla_s(\cdot) \equiv \mathbf{I}_s \cdot \nabla(\cdot)$, $\mathbf{I}_s = \mathbf{I} - \mathbf{kk}$, since thin layers and membranes behave like LCs, membranes should also exhibit flexoelectricity or couplings between polarization and bending [1–4,7,11,17–19]. Figure 2 shows a schematic of flexoelectric polarization in rod-like and banana-like molecules and the corresponding membrane flexoelectric polarization; as noted above the physics and modelling are affected by identifying the director field **n** with the membrane normal **k**.

Using the same approach as above, equation (1.4) gives the membrane polarization **P** due to membrane bending ($\nabla_s \cdot \mathbf{k}$):

$$\mathbf{P} = c_f(\nabla_s \cdot \mathbf{k})\mathbf{k}, \tag{1.10}$$

where c_f is the membrane flexoelectric coefficient, as indeed found experimentally [4]. The converse flexoelectric effect found from equation (1.5) gives the torque $\boldsymbol{\Gamma}$ due to an imposed

electric field

$$\mathbf{E} : \boldsymbol{\Gamma} = \mathbf{k} \times \{c_f[(\nabla_s \cdot \mathbf{k})\mathbf{E}_{//} - \nabla_s(\mathbf{k} \cdot \mathbf{E})]\}, \tag{1.11}$$

where $\mathbf{E}_{//} = (\mathbf{I} - \mathbf{kk}) \cdot \mathbf{E}$ is the tangential field. This equation shows that the converse flexoelectric effect in membranes exists when $c_f > 0$, and $\mathbf{E}_{//} \neq 0$ or $\nabla_s(\mathbf{k} \cdot \mathbf{E}) \neq 0$. Both the direct and converse membrane flexoelectric effects are sensor–actuator properties when membrane curvature and polarization are coupled as in nematic LCs. Membrane flexoelectricity due to its inherent sensor–actuator capabilities is an area of current interest in soft matter materials [1,7,8,14–24]. Over the years, much literature has dealt with the problem of measuring flexoelectric coefficients in various LCs [11,13]. For typical LC membranes, these coefficients range from 3 to 20 pC m^{-1}, but recent experiments have reported flexoelectricity coefficients of up to 35 nC m^{-1} in bent-core LCs [1–4,11,13]. Such large bend coefficients make bent-core LCs practical materials for mechano-electric transduction [11–13].

The specific objectives of this paper are

(1) to derive a high-order dynamic linear model for a flexoelectric membrane attached to a capillary tube that contains viscoelastic liquids and is subjected to a fluctuating small amplitude electric field of arbitrary frequency;
(2) to compute the frequency response of the electromechanical device, taking into account the viscoelastic nature of the contacting fluids;
(3) to use the modelling results to characterize the role of membrane flexoelectricity and contacting fluid viscoelasticity in the transfer function of the device; and
(4) to identify the material properties that lead to electromechanical conversion relevant to functioning of OHCs.

This paper is organized as follows. Section 2 introduces the generic features of the governing electro-rheological model of the electric field responsive membrane embedded in viscoelastic fluids. The governing equation is based on the integration of: (i) the flexoelectric membrane shape equation applied to a circular membrane attached to the inner surface of a circular capillary and (ii) the capillary flow of the contacting viscoelastic phases. Section 3 presents the actuation device model, dimensionless numbers, characteristic modes and the mechanical model analogue. Section 4 presents the block diagram, transfer functions, Kramers–Kronig equations and asymptotic values of the total transfer function. Section 5 presents the characteristic device functions: power output, membrane energy storage and Q-factor. Section 6 presents selected representative numerical results of the device functions. In §7, results are summarized. Appendix A presents the dimensionless numbers and appendix B the derivations of the Fourier transformations of the model and of the transfer functions.

2. Electro-rheological actuator model for flexoelectric membranes

To avoid repetition of lengthy derivations the reader is referred to a previous work [11], where we describe the fluid viscoelasticity with a Maxwell fluid model, neglect momentum inertia (zero Deborah number: $De = 0$) and formulate the model in the time domain. In this work, we model the system in the frequency domain, include momentum inertia, and develop a generic approach that can be used in the future with any viscoelastic constitutive equation, as required by experimental results. The physical set-up and geometry of the flexoelectric membrane tethered to a capillary tube containing two viscoelastic fluids is depicted in figure 3.

A capillary tube of radius a contains an edge-fixed flexoelectric membrane located at $z = 0$. Above and below the membrane there are two viscoelastic fluids with column heights $z = L$, viscosities $\{\eta_b, \eta_t\}$, relaxation times $\{\lambda_b, \lambda_t\}$ and densities $\{\rho_b, \rho_t\}$. The pressure at the top of the upper layer and at the bottom of the lower layer is equal to a constant, i.e. $p_t(\xi = 2L, t) = p_b(\xi = 0, t) = p_0$. By imposing a fluctuating electrical field $\mathbf{E}(t)$, the membrane oscillates and displaces the upper and lower incompressible viscoelastic fluids; we emphasize that the Poiseuille flow is only

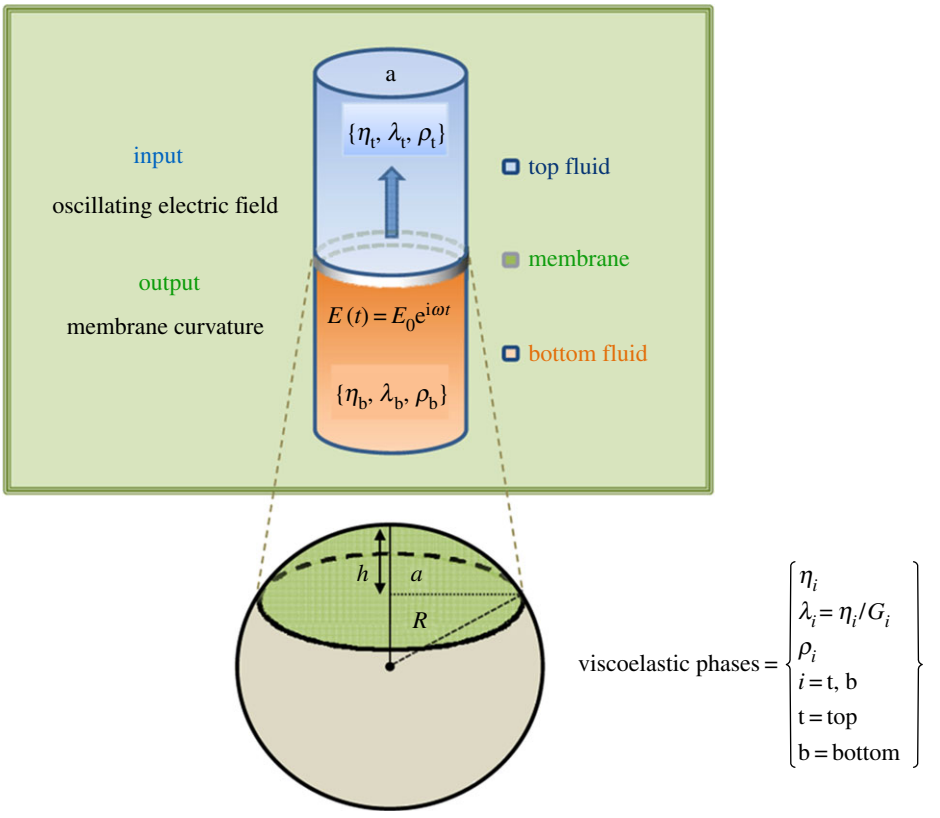

Figure 3. Schematic of the geometry and operation of flexoelectric mechanics, defined in figure 2, in a capillary geometry of radius a and axial length L. The input **E** field distorts the initially flat circular membrane into a spherical cap of radius R and height h. The flexoelectric actuation creates a capillary viscoelastic flow in the contacting top (t) and bottom (b) fluids of viscosities $\{\eta_t, \eta_b\}$, relaxation times $\{\lambda_t, \lambda_b\}$ and fluid densities $\{\rho_t, \rho_b\}$ (adapted from [11]). (Online version in colour.)

generated by the flexoelectric effect of the membrane caused by the imposed $\mathbf{E}(t)$ field [11,12]. The membrane deformation is described by a spherical dome of height h and radius R [12]. The shape equation that describes the average curvature $H(t)$ dynamics of the membrane is found by formulating the normal stress balance equation across the oscillating flexoelectric membrane [11–13]:

$$\underbrace{(c_f \Im) E(t)}_{\text{Input flexoelectric driving force}} = \underbrace{\Delta p(z = L, t)}_{\text{Bulk viscoelastic fluids' stress jump}} + \underbrace{(2\gamma_o + (2k_c + \bar{k}_c)\Im) H(t)}_{\text{Restoring membrane elastic force}}, \tag{2.1}$$

where the geometric factor $1/\Im = a^2/8$ indicates the characteristic deformation area associated with the spherical cup shown in figure 3 and $E = \mathbf{E} \cdot \mathbf{k}$. The shape equation (2.1) is a balance among membrane flexoelectric force, bulk viscoelastic liquid stress jump across the membrane and restoring membrane elastic force [11–13]. The oscillating flexoelectric force $\mathbf{F}_E(t)$

$$\mathbf{F}_E(t) = (c_f \Im) E(t) = c_f \left(\frac{8}{a^2} \right) \mathbf{E}(t) \tag{2.2}$$

is proportional to the externally imposed $\mathbf{E}(t)$ field and the flexoelectric coefficient c_f indicates the converse effect, through which $\mathbf{E}(t)$ creates the membrane vertical displacement [11–13]. As the membrane fluctuates, the contacting viscoelastic fluids dissipate and store energy through the oscillating upward and downward capillary flow [11–13]. The net vertical bulk force at the membrane $|\mathbf{kk} : \Delta \mathbf{T}_b|(t)$ contains both viscous and elastic contributions and is computed from the oscillatory viscoelastic capillary flow in a tube of total length $z = 2L$ [11].

Top fluid layer:

$$p_t(\xi = 2L, t) - p_t(\xi = z, t) = p_0 - p_t(\xi = z, t) = \left(\left(\frac{1}{r}\frac{\partial}{\partial r}r\right)\sigma_{rz}^{(t)} - \rho_t\frac{\partial v_z(r,t)}{\partial t}\right)(2L - z). \tag{2.3}$$

Bottom fluid layer:

$$p_b(\xi = z, t) - p_b(\xi = 0, t) = p_b(\xi = z, t) - p_0 = \left(\left(\frac{1}{r}\frac{\partial}{\partial r}r\right)\sigma_{rz}^{(b)} - \rho_b\frac{\partial v_z(r,t)}{\partial t}\right)z. \tag{2.4}$$

The pressure difference at $z = L$ is

$$\frac{\Delta p(z = L, t)}{L} = \frac{p_b(\xi = L, t) - p_t(\xi = L, t)}{L} = \left(\frac{1}{r}\frac{\partial}{\partial r}r\right)\sigma_{rz} - (\rho_t + \rho_b)\frac{\partial v_z(r,t)}{\partial t}, \tag{2.5}$$

where the total shear stress tensor σ_{rz} is the sum of the two viscoelastic phases:

$$\sigma_{rz} = \sigma_{rz}^{(t)} + \sigma_{rz}^{(b)} = \left(\frac{G_t\lambda_t}{1 + \lambda_t\partial_t} + \frac{G_b\lambda_b}{1 + \lambda_b\partial_t}\right)\frac{\partial v_z(r,t)}{\partial r} = \eta(t)\frac{\partial v_z(r,t)}{\partial r}, \tag{2.6}$$

where $\eta(t)$ can be considered as a time operator viscosity given by

$$\eta(t) = \frac{G_t\lambda_t}{1 + \lambda_t\partial_t} + \frac{G_b\lambda_b}{1 + \lambda_b\partial_t} = \frac{G_t\lambda_t + G_b\lambda_b + (G_t + G_b)\lambda_t\lambda_b\partial_t}{1 + (\lambda_t + \lambda_b)\partial_t + \lambda_t\lambda_b\partial_t^2}, \tag{2.7}$$

and $(\rho_t + p_b)$ is the total density (top and bottom fluids). In equation (2.6), the constitutive equation for the shear stress is given by the linear viscoelastic Maxwell model. The extension for higher models and fractional models can simply be done by just changing the mathematical differential operator given in equation (2.7). Notice that the stress jump is linear with L. Combining equations (2.5) and (2.6), we have

$$\Delta p(z = L, t) = L\left\{\eta(t)\left(\frac{1}{r}\frac{\partial}{\partial r}r\right)\frac{\partial}{\partial r} - (\rho_t + \rho_b)\frac{\partial}{\partial t}\right\}v_z(r,t). \tag{2.8}$$

The membrane elasticity gives rise to a restoring force proportional to the membrane average curvature $H(t) = -R^{-1}(t)$ [11–13]

$$\boldsymbol{F}_M(t) = (2\gamma_o + (2k_c + \bar{k}_c)\Im)H(t) = (4LM)H(t), \tag{2.9}$$

where $2\gamma_o + (2k_c + \bar{k}_c)\Im = 4LM$ is the effective membrane tension that includes the membrane tension γ_o, bending k_c and torsion $\bar{k}_c$ [11–13] from edge effects and M is the effective elastic force.

3. Device model

In this section we: (i) scale the model to elucidate the key parameter combinations that impact device performance, (ii) show that the mathematical model can be mapped onto a mechanical spring–dashpot model, (iii) describe the parametric restrictions inherent in the device, and (iv) classify the possible response modes according to physical properties (inertia, viscosity and elasticity).

(a) Membrane shape and fluid flow equations

By substituting equations (2.1) and (2.7) into (2.8), the following dimensionless membrane shape–fluid flow equation is obtained:

$$\left\{\left(\Sigma_{\bar{\eta}} + \bar{\lambda}_t\bar{\lambda}_b\frac{\partial}{\partial\bar{t}}\right)\frac{1}{\bar{r}}\frac{\partial}{\partial\bar{r}}\bar{r}\frac{\partial}{\partial\bar{r}} - De^2\left(1 + \frac{\partial}{\partial\bar{t}} + \bar{\lambda}_t\bar{\lambda}_b\frac{\partial^2}{\partial\bar{t}^2}\right)\frac{\partial}{\partial\bar{t}}\right\}\bar{v}_z(\bar{r},\bar{t})$$
$$= 4\left(1 + \frac{\partial}{\partial\bar{t}} + \bar{\lambda}_t\bar{\lambda}_b\frac{\partial^2}{\partial\bar{t}^2}\right)(a_0^*\bar{E}(\bar{t}) - \bar{M}\bar{H}(\bar{t})). \tag{3.1}$$

Scaling details are given in appendix A. The volumetric flow rate is linked by the speed average membrane curvature through

$$\Im(\bar{t}) = 2\int_0^1 \bar{v}_z(\bar{r}\bar{t})\bar{r} - \frac{1}{2}\frac{\mathrm{d}}{\mathrm{d}\bar{t}}\bar{H}(\bar{t}). \tag{3.2}$$

Equation (3.1) is a linear partial differential dimensionless equation that describes the spatio-temporal changes of the axial velocity $\bar{v}_z(\bar{r},\bar{t})$ as a function of the viscoelastic and flexoelectric material parameters in the system through dimensionless characteristic numbers associated with each physical mechanism. The first term on the left-hand side of equation (3.1) describes the viscous force and the second term is the momentum inertia force. The right-hand side is the flexoelectric force. Key features of this fluid pump device derived from equation (3.1) are: (i) at zero frequency the solid-like membrane response is $a_0^*\bar{E}(\bar{t}) - \bar{M}\bar{H}(\bar{t}) = 0$ and (ii) at infinite frequency the solid-like response is given by the balance between $De^2(\partial\bar{v}_z/\partial\bar{t}) = 4\bar{\lambda}_t\bar{\lambda}_b(\partial^2(a_0^*\bar{E}(\bar{t}) - \bar{M}\bar{H}(\bar{t}))/\partial\bar{t}^2)$. Hence membrane solid behaviour at large frequency only exists for $De > 0$. The mechanical response and energetic contributions of equation (3.1) were studied in [11], which now serves as reference to characterize the effects of De, which scales the inertia force $I(De, \bar{\lambda}_t\bar{\lambda}_b)$ generated by the flow kinematics:

$$I(De, \bar{\lambda}_t\bar{\lambda}_b) = De^2\left(\frac{\partial}{\partial\bar{t}} + \frac{\partial^2}{\partial\bar{t}^2} + \bar{\lambda}_t\bar{\lambda}_b\frac{\partial^3}{\partial\bar{t}^3}\right)\bar{v}_z(\bar{r},\bar{t}). \tag{3.3}$$

(b) Mechanical model

Here, we show that in the inertialess regime the model can be mapped into a standard mechanical spring–dashpot model. By neglecting the momentum inertia (small Deborah number, i.e. $De \geq 0$) in equation (3.1) and using equation (3.2), the following second-order linear differential equation is obtained:

$$\left\{b_2^*(k,\bar{\lambda}_t\bar{\lambda}_b)\frac{\mathrm{d}^2}{\mathrm{d}t^2} + b_1^*(k,\Sigma_{\bar{\eta}})\frac{\mathrm{d}}{\mathrm{d}t} + 1\right\}\bar{H}(\bar{t}) = a_0^*\frac{1-k}{k}\left\{kb_2^*(k,\bar{\lambda}_t\bar{\lambda}_b)\frac{\mathrm{d}^2}{\mathrm{d}t^2} + \frac{\mathrm{d}}{\mathrm{d}t} + 1\right\}\bar{E}(\bar{t}), \tag{3.4}$$

where $(1-k)/k$ is the inverse of the dimensionless effective membrane tension, i.e. $(1-k)/k = 1/\bar{M}$. The curvature viscous $b_1^*(k,\Sigma_{\bar{\eta}})$ and curvature inertial $b_2^*(k,\bar{\lambda}_t\bar{\lambda}_b)$ material functions are defined by

$$b_1^*(k,\Sigma_{\bar{\eta}}) = 1 + \left(\frac{1-k}{k}\right)\Sigma_{\bar{\eta}} \tag{3.5a}$$

and

$$b_2^*(k,\bar{\lambda}_t\bar{\lambda}_b) = \frac{\bar{\lambda}_t\bar{\lambda}_b}{k}. \tag{3.5b}$$

The electro-rheological model given by equations (3.4) and (3.5) was previously obtained by Dakka *et al*. [11] using a different mathematical approach. (See appendix A in [11].)

The device model given by equation (3.4) can be obtained directly by using a mechanical analogue as shown in figure 4, where curvature is mapped into strain and the electric field is mapped into stress. This new result provides a basis to incorporate more complex polymer rheology into the material aspects of the device. The deduction of the mechanical analogue model involves the derivation of the elastic and viscoelastic operators and its proper configuration.

The total electrical force in equation (3.4) is the sum of two viscoelastic contributions (springs and dashpots) and the flexoelectric membrane:

$$a_0^*\bar{E}(\bar{t}) = a_0^*\bar{E}(\bar{t})_{\mathrm{Maxwell-top}} + a_0^*\bar{E}(\bar{t})_{\mathrm{membrane}} + a_0^*\bar{E}(\bar{t})_{\mathrm{Maxwell-bottom}}. \tag{3.6}$$

The viscoelastic relationship between the electrical field and average membrane curvature for a Maxwell operator is

$$a_0^*\bar{E}(\bar{t}) = \left\{\bar{G}_t\bar{\lambda}_t\frac{\partial_{\bar{t}}}{1+\bar{\lambda}_t\partial_{\bar{t}}} + \bar{M} + \bar{G}_b\bar{\lambda}_b\frac{\partial_{\bar{t}}}{1+\bar{\lambda}_b\partial_{\bar{t}}}\right\}\bar{H}(\bar{t}). \tag{3.7}$$

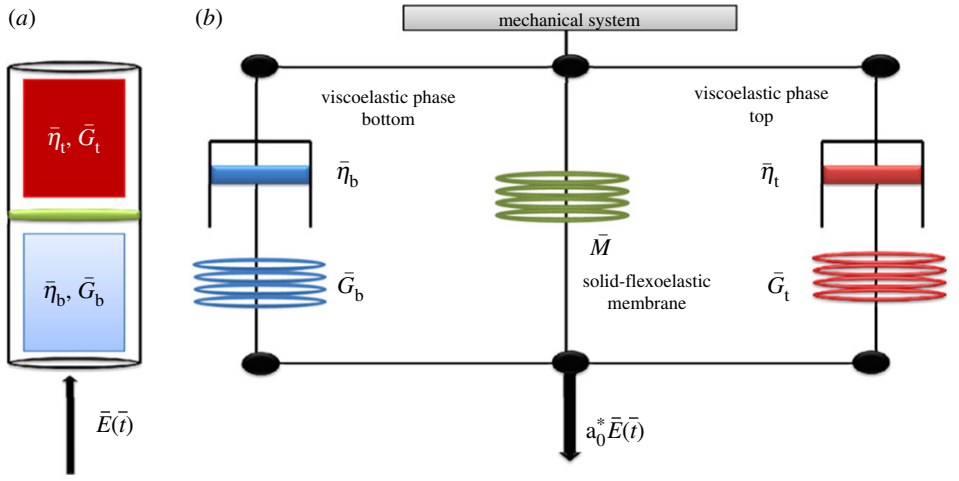

Figure 4. (*a*) Schematic of linear viscoelastic flexoelectric system represented by two viscoelastic fluids (red and blue) separated by an elastic membrane (green). (*b*) Mechanical analogue consisting of two Maxwell elements (top and bottom fluids) in parallel with an elastic spring (membrane). (Online version in colour.)

Multiplying equation (3.7) by the time linear operator $(1+\bar{\lambda}_t\partial_{\bar{t}})(1+\bar{\lambda}_b\partial_{\bar{t}})$ and using $(1-k)/k = 1/\bar{M}$, the second-order differential equation given by equations (3.4) and (3.5) is obtained. Placing the corresponding elements in parallel derived in equation (3.6) gives the mechanical model of figure 4.

In §4, we perform a Fourier analysis of equations (3.1) and (3.2), and establish the connections between the mathematical model, the mechanical model (figure 4) and the Fourier-based block diagram.

(c) Dimensionless numbers

The governing equation (3.1) contains five dimensionless numbers $\{\bar{\lambda}_t\bar{\lambda}_b, \Sigma_{\bar{\eta}}, k, De, a_0^*\}$ (see equations (A 1)–(A 10)) which are associated with the following mechanisms. (i) Memory ($\bar{\lambda}_t\bar{\lambda}_b$): product of the viscoelastic dimensionless times $\bar{\lambda}_t$ and $\bar{\lambda}_b$, it obeys $\bar{\lambda}_t + \bar{\lambda}_b = 1$ and defines the elastic asymmetry of the fluids. When $\bar{\lambda}_t\bar{\lambda}_b \ll 1$ (highly asymmetric case) one of the fluids is nearly inelastic and when $\bar{\lambda}_t\bar{\lambda}_b = 1/4$ (highly symmetric case) both fluids are equally elastic. (ii) Bulk viscosity ($\Sigma_{\bar{\eta}} = \bar{\eta}_t + \bar{\eta}_b = \bar{G}_t\bar{\lambda}_t + \bar{G}_b\bar{\lambda}_b$): total viscosity in the system, where the elastic dimensionless moduli satisfy $\bar{G}_t + \bar{G}_b = 1$. The numerical value of this number is controlled by the product between the two dimensionless Maxwell time numbers $\bar{\lambda}_t\bar{\lambda}_b$, $\Sigma_{\bar{\eta}} = \Sigma_{\bar{\eta}}(\bar{\lambda}_t\bar{\lambda}_b)$. (iii) Elastic ratio ($k$): dimensionless ratio between the membrane and the total system elasticity: $0 < k = (1+1/\bar{M})^{-1} < 1$. A floppy (soft) and stiff (rigid) membrane corresponds to $k \ll 1$ and $k \cong 1$, respectively. The elastic ratio, $k = k(\bar{M})$ is determined by the dimensionless elastic membrane modulus. (iv) and (v) The Deborah De and flexoelectric a_0^* numbers given by

$$De = \frac{t_i}{t_{ve}} = \frac{a\sqrt{(\rho_t+\rho_b)/(G_t+G_b)}}{\lambda_t+\lambda_b} \tag{3.8a}$$

and

$$a_0^* = \frac{c_f \Im E_0 a/4L}{M}. \tag{3.8b}$$

De is the ratio between the two time scales associated with inertia (t_i) and viscoelasticity (t_{ve}), and a_0^* is the dimensionless conversion of electric to elastic energy or equivalently the static transfer function at zero frequency.

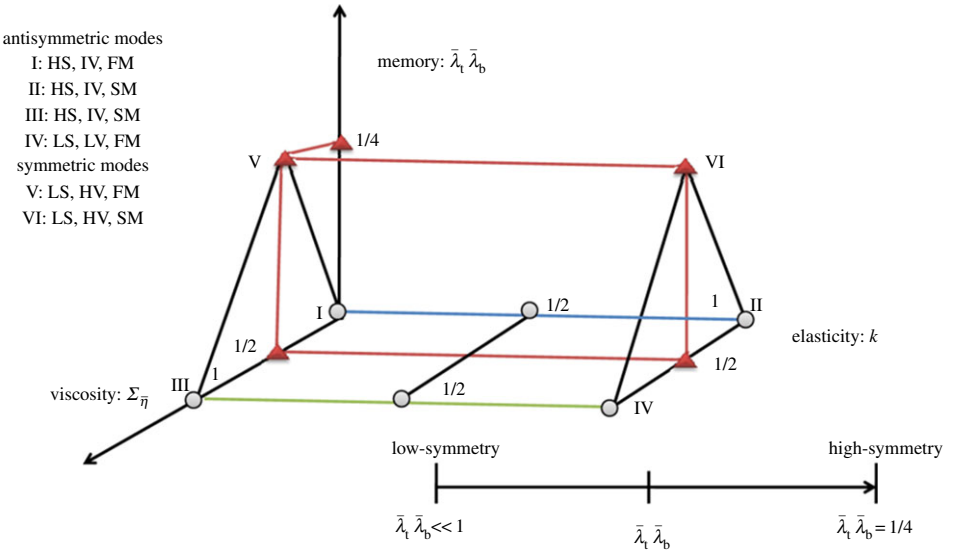

Figure 5. Prismatic material space for the six possible modes of equation (3.5), shown in table 1. The vertical axis is the memory of the fluids, the horizontal axis is the elasticity ratio k, and the axis into the page is the total viscosity of the fluids. The six vertices correspond to the six modes in table 1. (Online version in colour.)

Table 1. Device response modes. $\bar{\lambda}_t\bar{\lambda}_b$, memory; $\Sigma_{\bar{\eta}}$, viscosity; k, elasticity ratio; $\boldsymbol{\varepsilon \approx 0(10^{-4})}$.

system's modes	$\bar{\lambda}_t\bar{\lambda}_b$	$\Sigma_{\bar{\eta}} = \Sigma_{\bar{\eta}}(\bar{\lambda}_t\bar{\lambda}_b)$	k
(I) low symmetry, low viscosity, floppy membrane {LS, LV, FM}	ε	ε	$k \ll 1$ $k \cong \varepsilon$
(II) low symmetry, low viscosity, stiff membrane {LS, LV, SM}	ε	ε	1
(III) low symmetry, high viscosity, floppy membrane {LS, HV, FM}	ε	$1-\varepsilon$	$k \ll 1$ $k \cong \varepsilon$
(IV) low symmetry, high viscosity, stiff membrane {LS, HV, SM}	ε	$1-\varepsilon$	1
(V) high symmetry, intermediate viscosity, floppy membrane {HS, IV, FM}	1/4	1/2	$k \ll 1$
(VI) high symmetry, intermediate viscosity, stiff membrane {HS, IV, SM}	1/4	1/2	1

(d) Response mode classification

To satisfy equations (3.1)–(3.5), besides the restrictions noted above, the maxima and minima values of the total dimensionless bulk viscosity number $(\Sigma_{\bar{\eta}_{\min}}, \Sigma_{\bar{\eta}_{\max}})$ must be bounded by the values of the Maxwell relaxation times in the bottom and the top fluids. Under perfect symmetry (identical elasticity in top and bottom fluids) $\bar{\lambda}_t\bar{\lambda}_b = 1/4$, and the total viscosity is fixed at $\Sigma_{\bar{\eta}_{\max}} = \Sigma_{\bar{\eta}_{\min}} = 0.5$, while under nearly total asymmetry $\bar{\lambda}_t\bar{\lambda}_b \approx \varepsilon \ll 1$, the total viscosity can vary between $\Sigma_{\bar{\eta}_{\max}} = 1$, $\Sigma_{\bar{\eta}_{\min}} = \varepsilon \ll 1$. According to the magnitudes of the three dimensionless numbers $\{\bar{\lambda}_t\bar{\lambda}_b, \Sigma_{\bar{\eta}}, k\}$, the system (equation (3.2)) displays six distinct modes, summarized in table 1. These six modes arise since the memory symmetry can be high (HS) or low (LS), the total viscosity high (HV), intermediate (IV) or low (LV), and the membrane can be floppy (FM) or stiff (SM). For example, in table 1 the third row mode {LS, LV, FM} corresponds to low symmetry, low viscosity and floppy membrane. This effective mode classification narrows down the parametric envelope of biological significance.

The specific numerical values in table 1 are selected as to be characteristic of each mode. The six modes in table 1 can be represented by the vertices of a prismatic three-dimensional material

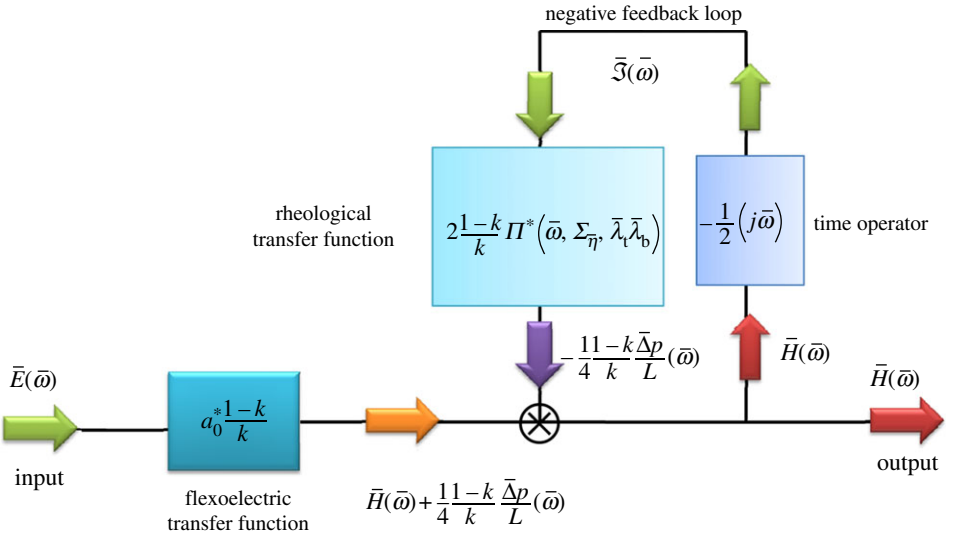

Figure 6. The dynamic control process for the flexoelectric membrane embedded in the two viscoelastic media. Notice that the negative feedback control eliminates the pressure gradient. (Online version in colour.)

space shown in figure 5, spanned by fluid memory $\{\bar{\lambda}_t\bar{\lambda}_b\}$, membrane elasticity $\{k\}$ and total fluid viscosity $\{\Sigma_{\bar{\eta}}\}$. The front edge of the prism, defined by the line $\bar{\lambda}_t\bar{\lambda}_b = 10^{-4}$, $\Sigma_{\bar{\eta}} = 1$, $0 < k < 1$. In §4, we will report the role of *De*. Earlier, we worked without inertia [11] and we have established that mode III is the most relevant to the functioning of OHCs.

Flow field characterization and visualization of importance to biophysical applications is left to future work.

4. Transfer functions and block diagram

In this section, we derive the energy conversion device block diagram and the transfer functions involved in converting the **E**-field into viscoelastic flow. The derivations involve using the Fourier transform to solve the governing equations (3.1) and (3.2) and details are shown in appendix B. We also demonstrate that the total transfer function follows from the Kramers–Kronig relations.

Block diagrams are useful tools to characterize complex dynamical systems. Taking the Fourier transform of equations (2.9)–(3.2) and (3.4) yields the block diagram shown in figure 6. The membrane shape–fluid flow coupling is a negative feedback loop in the block diagram of the device. Appendix B shows derivation details and symbol definitions. The diagram shows how the input $\bar{E}(\bar{\omega})$ creates the output $\bar{H}(\bar{\omega})$ by the action of a negative feedback that emerges because as the membrane fluctuates it creates both membrane curvature and fluid flow $\bar{\Im}(\bar{\omega})$ which exactly balances the pressure drop $((1-k)/k)(\overline{\Delta p}/L)/4$ across the membrane. Next, we discuss the three elements shown in the block diagram (figure 6): (i) flexoelectric transfer function $(a_0^*(1-k)/k)$, (ii) time operator $(-(j\bar{\omega})/2)$, and (iii) rheological transfer function $(2(1-k)\bar{\Pi}(\bar{\omega})/k)$.

(a) Flexoelectric transfer function

The flexoelectric transfer function $a_0^*(1-k)/k$ converts the $\bar{E}$ input into membrane curvature $\bar{H}$ and a pressure drop $((1-k)/k)(\overline{\Delta p}/L)/4$

$$\underbrace{\bar{E}(\bar{\omega})}_{\text{Input}}\left\{a_0^*\frac{1-k}{k}\right\} = \underbrace{\bar{H}(\bar{\omega}) + \frac{1}{4}\frac{1-k}{k}\frac{\overline{\Delta p}}{L}(\bar{\omega})}_{\text{Output}}. \tag{4.1}$$

This transfer function is the product of the bare flexoelectric coefficient a_0^* and the elasticity of the fluids $(1-k)/k$ since conversion depends on the effective elasticity.

(b) Differential operator

The speed of membrane curvature is the volumetric flow rate

$$\underbrace{-\frac{1}{2}(j\bar{\omega})\bar{H}(\bar{\omega})}_{\text{Membrane speed}} = \underbrace{\bar{\Im}(\bar{\omega})}_{\text{Flow rate}}, \tag{4.2}$$

as per equation (3.2). This block is a derivative operator which converts the kinetics of the membrane into a capillary flow and is the first component of the feedback loop.

(c) Rheological transfer function

The second component of the feedback loop is the rheological transfer function. The evolution of the membrane curvature causes a volumetric flow, which is regulated by the viscoelastic mechanism through a material viscosity function:

$$\underbrace{\bar{\Im}(\bar{\omega})}_{\text{Input}} \underbrace{\left\{2\frac{1-k}{k}\bar{\Pi}(\bar{\omega})\right\}}_{\substack{\text{Rheological}\\ \text{transfer function}}} = \underbrace{\left(-\frac{1}{4}\frac{1-k}{k}\frac{\overline{\Delta p}}{L}(\bar{\omega})\right)}_{\text{Output}}, \tag{4.3a}$$

where the viscosity functional $\bar{\Pi}$ is given by (see equation (B 6*b*))

$$\bar{\Pi}(\bar{\omega},\beta) = -De^2(j\bar{\omega}) \Big/ 32\left(1-2\frac{J_1(\beta)/\beta}{J_0(\beta)}\right), \tag{4.3b}$$

where J_0 and J_1 are Bessel functions. Combining equations (4.1)–(4.3), the relation between the average membrane curvature as a function of the applied electrical field is found to be

$$\bar{H}(\bar{\omega}) = \left\{\frac{(1-k)/k}{1+(1-k)/k\bar{\Pi}(\bar{\omega},\beta)\cdot(j\bar{\omega})}\right\}\bar{E}(\bar{\omega}). \tag{4.4}$$

(d) Total transfer function

From equation (4.4), the total transfer function $F_D(\bar{\omega})$ is found to be (appendix B)

$$F_D(\bar{\omega}) = \mathrm{Re}[F_D(\bar{\omega})] + j\mathrm{Im}[F_D(\bar{\omega})] = \frac{\bar{H}(\bar{\omega})}{\bar{E}(\bar{\omega})} = a_0^*\frac{((1-k)/k)X(\bar{\omega};\beta)}{((1-k)/k)+X(\bar{\omega};\beta)} = F_S\frac{X(\bar{\omega};\beta)}{((1-k)/k)+X(\bar{\omega};\beta)}, \tag{4.5}$$

where $F_S = a_0^*((1-k)/k)$ is the static transfer function. $X(\bar{\omega};\beta) = \bar{\Pi}(\bar{\omega};\beta)\cdot(j\bar{\omega})$ is a complex function of the Deborah number, the frequency, and the real and imaginary parts of the fluidities (inverse of the viscosities), and can expressed in terms of a power series:

$$X(\bar{\omega};\beta) = \mathrm{Re}[X(\bar{\omega};\beta)] + j\mathrm{Im}[X(\bar{\omega};\beta)] = \sum_{k=1}^{N}\delta_k(De^2)^{k-1}\cdot(\bar{\omega})^{k-2}(j^3)^k(\varphi(\bar{\omega}))^k. \tag{4.6}$$

Combining equations (4.5) and (4.6), the following compact form of the transfer function $F_D(\bar{\omega})$ is obtained:

$$F_D(\bar{\omega}) = F_S\frac{\sum_{k=1}^{N}\delta_k(De^2)^{k-1}(\bar{\omega})^{k-2}(j^3)^k(\varphi(\bar{\omega}))^k}{((1-k)/k)+\sum_{k=1}^{N}\delta_k(De^2)^{k-1}(\bar{\omega})^{k-2}(j^3)^k(\varphi(\bar{\omega}))^k}, \tag{4.7}$$

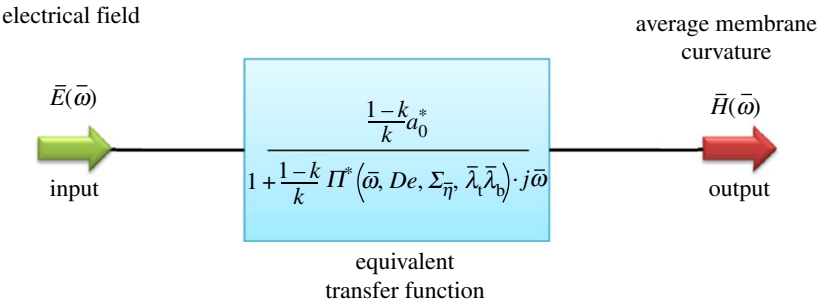

Figure 7. Effective block diagram for the flexoelectric membrane embedded in two viscoelastic media. The total transfer function integrates the flexoelectric and rheological transfer functions shown in figure 6 and its format reflects the negative feedback loop in figure 5. (Online version in colour.)

where the coefficients δ_k are real negative numbers (see appendix B). The convergence of the power series of equation (4.7) is slow; however, we are interested in a small contribution of the inertial mechanisms, so for $N = 2$, the system exhibits a resonance effect.

The total transfer function given by equation (4.5) can now be represented in an equivalent simpler block diagram shown in figure 7.

In equations (4.6) and (4.7), the complex fluidity $\varphi(\bar{\omega}) = \mathrm{Re}[\varphi(\bar{\omega})] + j\mathrm{Im}[\varphi(\bar{\omega})]$ is given by

$$\varphi(\bar{\omega}) = \frac{1 + (j\bar{\omega}) + \bar{\lambda}_t\bar{\lambda}_b(j\bar{\omega})^2}{\Sigma_{\bar{\eta}} + \bar{\lambda}_t\bar{\lambda}_b(j\bar{\omega})} = \frac{\Sigma_{\bar{\eta}} + (1 - \Sigma_{\bar{\eta}})\bar{\lambda}_t\bar{\lambda}_b\bar{\omega}^2}{(\Sigma_{\bar{\eta}})^2 + (\bar{\lambda}_t\bar{\lambda}_b\bar{\omega})^2} + j\left(\frac{\Sigma_{\bar{\eta}} - \bar{\lambda}_t\bar{\lambda}_b + (\bar{\lambda}_t\bar{\lambda}_b\bar{\omega})^2}{(\Sigma_{\bar{\eta}})^2 + (\bar{\lambda}_t\bar{\lambda}_b\bar{\omega})^2}\right)\bar{\omega}. \tag{4.8}$$

The real and imaginary parts of the fluidity are positive $\{Re[\varphi(\bar{\omega})] > 0, \mathrm{Im}[\varphi(\bar{\omega}) > 0]\}$. Equations (4.7) and (4.8) are new findings of this work, and the starting point to characterize OHCs. The flexoelectric transfer function $F_D(\bar{\omega})$ depends on the elastic ratio k, Deborah number De, and the real and imaginary parts of the fluidity $\varphi(\bar{\omega})$ which is determined by specific physical mechanisms through the dimensionless numbers defined in §2.

(e) Kramers–Kronig relations

In this section, we show that equations (4.5) and (4.6) obey the well-known Kramers–Kronig dispersion relations, which have significant applicability in real systems since they relate real and imaginary components of the transfer function. Thus the real and imaginary parts of the transfer function given by equation (4.5) are given by

$$\begin{aligned}\mathrm{Re}[F_D(\bar{\omega})] &= \frac{2}{\pi}P\int_0^{+\infty}\frac{\bar{\omega}'\mathrm{Im}[F_D(\bar{\omega}')]}{\bar{\omega}'^2 - \bar{\omega}^2}\mathrm{d}\bar{\omega}' \\ &= F_S\left\{\frac{1 + ((1-k)/k)\mathrm{Re}[X(\bar{\omega};\beta)]}{(1 + ((1-k)/k)\mathrm{Re}[X(\bar{\omega};\beta)])^2 + (((1-k)/k)\mathrm{Im}[X(\bar{\omega};\beta)])^2}\right\} \end{aligned} \tag{4.9}$$

$$\begin{aligned}\mathrm{Im}[F_D(\bar{\omega}')] &= \frac{2\bar{\omega}}{\pi}P\int_0^{+\infty}\frac{\bar{\omega}'\mathrm{Re}[F_D(\bar{\omega}')]}{\bar{\omega}'^2 - \bar{\omega}^2}\mathrm{d}\bar{\omega}' \\ &= F_S\left\{\frac{((1-k)/k)\mathrm{Im}[X(\bar{\omega};\beta)]}{(1 + ((1-k)/k)\mathrm{Re}[X(\bar{\omega};\beta)])^2 + (((1-k)/k)\mathrm{Im}[X(\bar{\omega};\beta)])^2}\right\}. \end{aligned} \tag{4.10}$$

In equations (4.9) and (4.10), P is the Cauchy principal value. These two equations are the dispersion relations for $F_D(\bar{\omega})$. For this system, the real and imaginary parts of the transfer function are analytical and can be expressed through equations (4.9) and (4.10).

We note the following limiting regimes:

Large Deborah numbers: when the inertia mechanisms are larger ($De \gg 1$) the transfer function has the following asymptotic expression: $\mathrm{Lim}_{De\to\infty}F_D(\bar{\omega}) \to F_S = a_0^*((1-k)/k)$.

Small Deborah numbers: the complex function $\bar{\Pi}(\bar{\omega},\beta)$ reduces to the total viscoelastic function, i.e. $\lim_{De\to 0}\bar{\Pi}(\bar{\omega},\beta)\to\bar{\eta}(\bar{\omega})=1/\bar{\varphi}(\bar{\omega})$ given by equation (4.8). The feedback loop system given by equations (4.4)–(4.7) and figure 7 can be simplified to a simpler system given in terms of the electrical field (input) and average membrane curvature (output) and its equivalent transfer function given by

$$F_{\mathrm{D}}(\bar{\omega})=\frac{a_0^*(1-k)/k}{1+(1-k)/k\bar{\eta}^*(\bar{\omega})\cdot(j\bar{\omega})}=\frac{a_0^*(1-k)/k}{1+(1-k)/k\bar{G}^*(\bar{\omega})}. \tag{4.11}$$

In equation (4.11), $\bar{G}^*(\bar{\omega})=\bar{\eta}^*(\bar{\omega})\cdot(j\bar{\omega})$ is the complex modulus. At small elastic ratio, $k\ll 1$, and without inertial effects, equation (4.11) takes the following asymptotic form:

$$\lim_{k\to 0}F_{\mathrm{D}}(\bar{\omega})=\lim_{k\to 0}\frac{a_0^*(1-k)/k}{1+((1-k)/k)\bar{G}^*(\bar{\omega})}\cong\frac{a_0^*}{\bar{G}^*(\bar{\omega})}=\frac{1}{\bar{G}^*(\bar{\omega})}\cong a_0^*J^*(\bar{\omega}), \tag{4.12}$$

where is $J^*(\bar{\omega})$ the compliance. The last equation implies that in the modes (I, III, V: floppy membrane) the response function is given by the product between the flexoelectric and flow-rheology mechanism (compliance) $F_{\mathrm{D}}(\bar{\omega})\equiv a_0^*J^*(\bar{\omega})$.

5. Device characterizing functions: curvature, power and *Q*-factor

In this section, we use the transfer functions derived in §4 to express the equations that govern the membrane curvature, the fluid power and the *Q*-factor.

(a) Membrane curvature

The membrane shape $\bar{H}(\bar{\omega}^*)$ responds to a complex exponential oscillatory electric field $\bar{E}(\bar{t},\bar{\omega}^*)=\exp(j\bar{\omega}^*\bar{t})$. The Fourier transform $\bar{E}(\bar{t},\bar{\omega}^*)=\exp(j\bar{\omega}^*\bar{t})$ can be expressed as a delta Dirac function, i.e. $\bar{E}(\bar{\omega}^*)=\delta(\bar{\omega}-\bar{\omega}^*)$, so the average membrane curvature in the Fourier domain is given by $\bar{H}(\bar{\omega}^*)=F_{\mathrm{D}}(\bar{\omega}^*)\delta(\bar{\omega}-\bar{\omega}^*)$. Finally, taking the inverse Fourier transform of the average membrane curvature, we have

$$\bar{H}(\bar{t},\bar{\omega})=\mathrm{Re}[\bar{H}(\bar{t},\bar{\omega})]+j\mathrm{Im}[\bar{H}(\bar{t},\bar{\omega})]=F_{\mathrm{D}}(\bar{\omega})\exp(j\bar{\omega}\bar{t}). \tag{5.1}$$

The curvature moduli can be calculated from equation (4.5), so the real and imaginary parts of the membrane curvature are given as follows:

$$\mathrm{Re}[\bar{H}(\bar{t},\bar{\omega})]=\mathrm{Re}[F_{\mathrm{D}}(\bar{\omega})]\cos(\bar{\omega}\bar{t})+\mathrm{Im}[F_{\mathrm{D}}(\bar{\omega})]\sin(\bar{\omega}\bar{t}) \tag{5.2}$$

and

$$\mathrm{Im}[\bar{H}(\bar{t},\bar{\omega})]=\mathrm{Im}[F_{\mathrm{D}}(\bar{\omega})]\cos(\bar{\omega}\bar{t})-\mathrm{Re}[F_{\mathrm{D}}(\bar{\omega})]\sin(\bar{\omega}\bar{t}). \tag{5.3}$$

For physical reasons, we are interested only in the real part of the average curvature function $\bar{H}(\bar{t},\bar{\omega})$, so for the rest of the paper, the imaginary part of equation (5.2) is not taken into account.

(b) Fluid power dissipation and membrane elastic storage

The key quantities for the device are the mechanical power delivered to the viscoelastic fluids $\bar{P}(\bar{\omega})$, the stored membrane elastic energy $\bar{E}m(\bar{\omega})$ due to curvature and the ratio of these two quantities, known as the *Q*-factor. The average power delivered to the viscoelastic fluids $\bar{P}(\bar{\omega})$ by the oscillating membrane is the period average of the product of the input force $\bar{E}(\bar{t},\bar{\omega})$ times

the flow rate $\bar{\Im}(\bar{t},\bar{\omega}) = -2^{-1}\mathrm{d}\bar{H}(\bar{t},\bar{\omega})/\mathrm{d}\bar{t}$ and is proportional to $\mathrm{Im}[F_{\mathrm{D}}(\bar{\omega})]$:

$$\bar{P}(\bar{\omega}) = \left\langle \mathrm{Re}\left[\bar{E}(\bar{t},\bar{\omega})\right] \cdot \mathrm{Re}\left[\bar{\Im}(\bar{t},\bar{\omega})\right]\right\rangle = \frac{1}{2}\bar{\omega}\left|\mathrm{Im}\left[F_{\mathrm{D}}(\bar{\omega})\right]\right|. \tag{5.4}$$

The period average elastic membrane energy $\bar{E}m(\bar{\omega}) = \langle \mathrm{Re}[\bar{H}(\bar{t},\bar{\omega})] \cdot \mathrm{Re}[\bar{H}(\bar{t},\bar{\omega})]\rangle$ indicates the amount of energy stored by bending and is proportional to $|F_{\mathrm{D}}(\bar{\omega})|^2$:

$$\bar{E}m(\bar{\omega}) = \langle(\mathrm{Re}[\bar{H}(\bar{t},\bar{\omega})])^2\rangle = \frac{1}{2}\{(\mathrm{Re}[F_{\mathrm{D}}(\bar{\omega})])^2 + (\mathrm{Im}[F_{\mathrm{D}}(\bar{\omega})])^2\}. \tag{5.5}$$

The Q-factor is the ratio between stored elastic membrane energy $\bar{E}(\bar{\omega})$ and the power delivered to the viscoelastic fluids $\bar{P}(\bar{\omega})$ by the oscillating membrane and is proportional to $\mathrm{Re}[F_{\mathrm{D}}(\bar{\omega})] \cdot \cot\phi + \mathrm{Im}[F_{\mathrm{D}}(\bar{\omega})]$:

$$Q(\bar{\omega}) = \frac{\bar{E}m(\bar{\omega})}{\bar{P}(\bar{\omega})} = \frac{1}{\bar{\omega}}\{\mathrm{Re}[F_{\mathrm{D}}(\bar{\omega})]\cot\phi + \mathrm{Im}[F_{\mathrm{D}}(\bar{\omega})]\}, \tag{5.6}$$

where the phase angle ϕ is defined in equation (1.3). The Q-factor is a measure of the relative importance of dissipative and storage processes, and depends on the inertia, memory of the two viscoelastic phases, bulk viscosity, elastic ratio and flexoelectric mechanisms, through the dimensionless numbers $\{\bar{\lambda}_{\mathrm{t}}\bar{\lambda}_{\mathrm{b}}, \Sigma_{\bar{\eta}}, k, a_0^*, De\}$. The magnitude of the Q-factor defines two important regimes $\{Q(\bar{\omega}) > 1; Q(\bar{\omega}) < 1\}$:

$$Q(\bar{\omega}) = \begin{cases} Q(\bar{\omega}) > 1 : \text{membrane elastic storage} > \text{fluid power} \\ Q(\bar{\omega}) = 1 : \text{membrane elastic storage} = \text{fluid power} \\ Q(\bar{\omega}) < 1 : \text{membrane elastic storage} < \text{fluid power (biological zone).} \end{cases} \tag{5.7}$$

In [11], it was shown that the $Q(\bar{\omega}) < 1$ biological zone relevant to the functioning of OHCs was found in mode III (table 1) associated with maximum viscosity, high contrast between the viscoelastic contacting phases and small elastic ratio. In the next section, the membratodynamic model is extended taking into account the inertial mechanism using the transfer function approach.

6. Numerical results

This section presents the mechanical response (computed using equations (4.7), (4.8), (5.1)–(5.6)), fluid dissipation, membrane elastic storage and Q-factor as a function of the dimensionless frequency. The main objective is to identify material conditions that lead to a biologically relevant power spectrum with a well-defined resonant peak and Q-factor less than one ($Q(\bar{\omega}) < 1$), using the transfer function methodology of §§4 and 5.

Table 2 presents a summary of the main features of the frequency response of $\mathrm{Re}[F_{\mathrm{D}}(\bar{\omega})], \mathrm{Im}[F_{\mathrm{D}}(\bar{\omega})], \bar{P}(\bar{\omega}), \bar{E}m(\bar{\omega}), Q(\bar{\omega})$, under zero inertia ($De = 0$) and with inertia ($De > 0$) for the modes {I, III, V} identified in figure 5; the other modes {II, IV, VI} corresponding to stiff (large k) membranes are not biologically relevant [18] either because they do not form power peaks or because $Q(\bar{\omega}) > 1$ (store more membrane elastic energy than inject momentum into the fluids). In the case when the inertial mechanisms are neglected, $De \ll 1$, the real $\mathrm{Re}[F_{\mathrm{D}}(\bar{\omega})]$ and imaginary $\mathrm{Im}[F_{\mathrm{D}}(\bar{\omega})]$ parts of the transfer function behave as would be expected for a simple viscoelastic system displaying a single peak and two asymptotic plateaus separated by a power-law region (PLR). On the other hand, the power dissipation $\bar{P}(\bar{\omega})$ shows a monotonically increasing behaviour followed by a plateau. It will be shown that under no inertia ($De = 0$) the power $\bar{P}(\bar{\omega})$ only shows a well-formed peak for mode III {LS, HV, FM} while all the other modes (I, V) do not. The elastic energy $\bar{E}m(\bar{\omega})$ shows a solid behaviour (whose range and magnitude depends on k) at low frequency and then a power-law behaviour with frequency for all modes. The Q-factor which is an index of merit for power delivery, decreases with frequency and eventually achieves a plateau in all cases, except again for mode III {LS, HV, FM}, where it eventually increases with dimensionless frequency. This tabular summary of generic dissipated

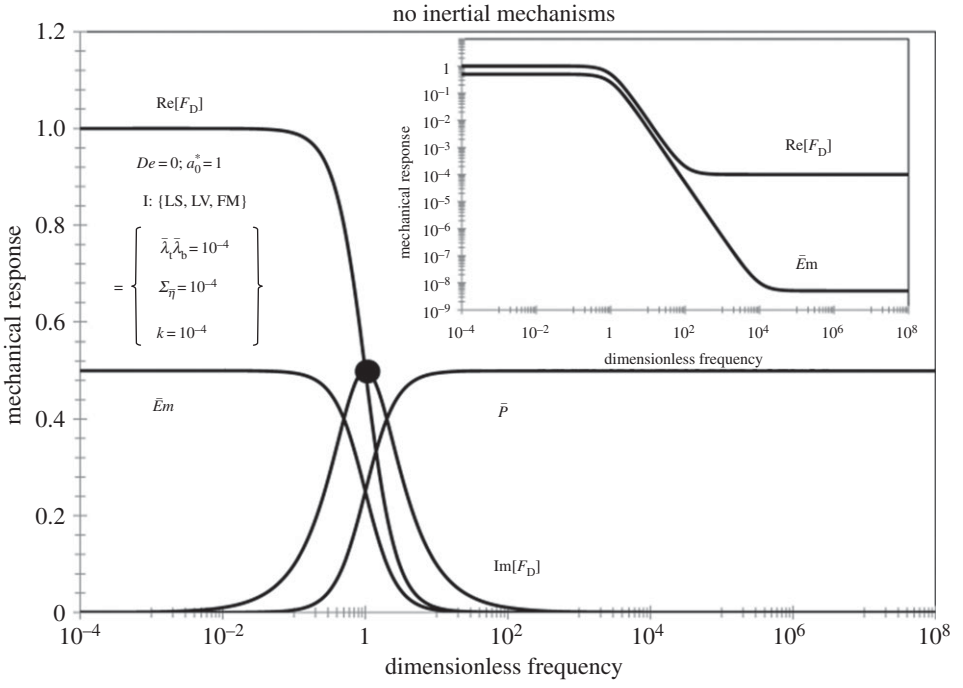

Figure 8. Mechanical response: Re[$F_D(\bar{\omega})$], Im[$F_D(\bar{\omega})$], $\bar{P}(\bar{\omega})$, $\bar{E}m(\bar{\omega})$, $Q(\bar{\omega})$ as a function of dimensionless frequency $\bar{\omega}$, for mode I in table 1 {LS, LV, FM} and $De = 0$. The response is elastic at low frequency, viscous at high frequency and viscoelastic at intermediate frequencies. The black dot corresponds to the cross-over frequency.

power and stored energy features proves most useful to narrow the parametric envelopes relevant to the biological performance of this device.

Figure 8 shows the mechanical response as a function of frequency for mode I, for $De = 0$. The transfer function behaves as a classical viscoelastic system, with the real part displaying low- and high-frequency plateaus and with a pulse in the imaginary part. The membrane behaves as a solid at low frequency and the power increases with frequency and fails to display a resonant plateau.

Figure 9 shows the frequency response when the inertial mechanisms are present. The real part of the transfer function shows a single broad well. The imaginary part of the transfer function shows a classical resonance behaviour with two single peaks. It is found that inertia ($De > 0$) leads to a resonance behaviour in modes {I, III, V}, while table 2 shows that for $De = 0$ only mode III displays a well-formed power peak.

The power shows a single peak at high dimensionless frequency, and the elastic energy shows a single sharp peak profile.

(a) Fluid power dissipation and membrane energy storage

Figure 10 shows the power dissipation $\bar{P}(\bar{\omega})$ as a function of the dimensionless frequency $\bar{\omega}$ for the modes {I, III, V}, with inertia $De \neq 0$ (figure 10*a*) and without inertia $De = 0$ (figure 10*b*). Inertia generates well-localized resonant peaks in the three modes (I, II, III). Inertialess conditions generate a broader power peak only in mode III (large viscosity) since dissipative modes persist with higher frequencies. These facts follow from the fact that the power is proportional to the imaginary part of the transfer function $\bar{P}(\bar{\omega}) = |\mathrm{Im}[F_D(\bar{\omega})]|/2$ (see equation (4.9)) and according to the asymptotic results of appendix C, only under finite inertia Im[$F_D(\bar{\omega})$] converges at large frequency to its static value. Hence, except for mode III, inertialess conditions do not generate power pulses.

Table 2. Frequency response: Re[$F_D(\bar{\omega})$], Im[$F_D(\bar{\omega})$], $\bar{P}(\bar{\omega})$, $\bar{Em}(\bar{\omega})$, $Q(\bar{\omega})$. ↓, Decrease its amplitude value; ←, frequency left shift.

mode	Re[F_D]	Im[F_D]	P	Em	Q
$De = 0$					
I{LS, LV, FM}	two plateaus at low and high frequencies and PLR	single pulse with the maximum peak centred in the resonance frequency	linear increasing behaviour to follow of an asymptotic value	two plateaus at low and high frequencies and PLR ←	linear decreasing asymptotic value $Q \ll 1$
III{LS, HV, FM}	two plateaus at low and high frequencies and PLR ←	↓ single pulse with the maximum peak centred in the resonance frequency ←	single pulse with the maximum peak centred in a particular resonance frequency. *Biological zone*	two plateaus at low and high frequencies and PLR ←	linear decreasing asymptotic value $Q \gg 1$
V{HS, IV, FM}	two plateaus at low and high frequencies and PLR ←	linear decreasing in all the frequency range	↓ linear increasing behaviour to follow of an asymptotic value	two plateaus at low and high frequencies and PLR ←	linear decreasing asymptotic value $Q \gg 1$
$De \neq 0$					
I{LS, LV, FM}	two plateaus at low and high frequencies and PLR. Constant value followed of an increasing behaviour until a plateau	first pulse with the maximum peak centred in the resonance frequency, followed of a second single pulse. The value of the maximum second peak is less than the first peak	↑ single pulse with the maximum peak centred in a particular resonance frequency	two plateaus at low and high frequencies and PLR. Constant value followed of an increasing behaviour until a plateau	linear decreasing asymptotic value, increasing behaviour $Q \ll 1$
III{LS, HV, FM}	same behaviour in the mode {*I*, *III*} except that all the curves are shifted to the left to small dimensionless frequency ←	same behaviour in the mode I, except that all the curves are shifted to the left to small dimensionless frequency ←	↓ single pulse with the maximum peak centred in a particular resonance frequency	two plateaus at low and high frequencies and PLR. Constant value followed of an increasing behaviour until a plateau	linear decreasing asymptotic value, increasing behaviour $Q \gg 1$
V{HS, IV, FM}	same behaviour in the modes {*I*, *III*} except that all the curves are shifted to the left to small dimensionless frequency ←	same behaviour in the modes {*I*, *III*} except that all the curves are shifted to the left to small dimensionless frequency ←	↓ single pulse with the maximum peak centred in a particular resonance frequency	linear behaviour	linear decreasing asymptotic value, increasing behaviour $Q \gg 1$

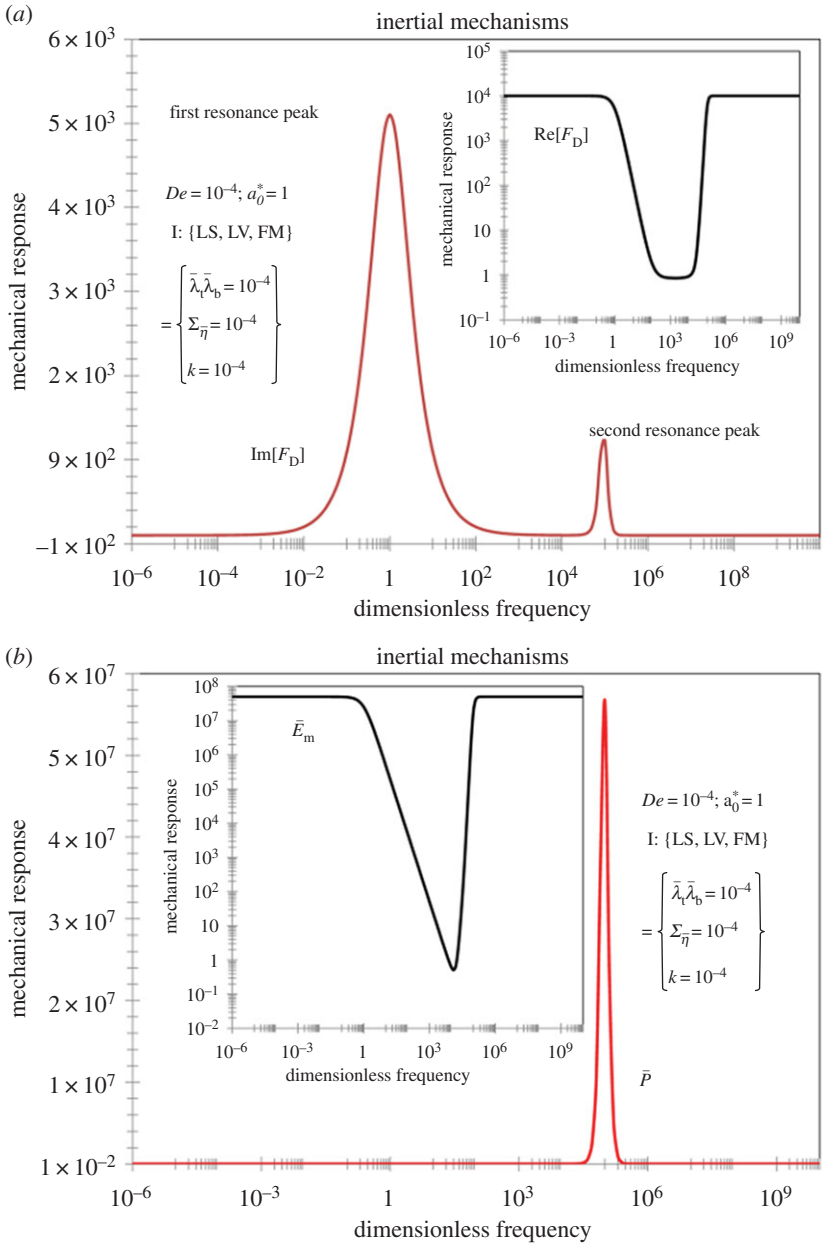

Figure 9. Mechanical response: $\mathrm{Re}[F_D(\bar{\omega})]$, $\mathrm{Im}[F_D(\bar{\omega})]$, $\bar{P}(\bar{\omega})$, $\bar{E}m(\bar{\omega})$, $Q(\bar{\omega})$ as a function of dimensionless frequency $\bar{\omega}$ for mode I in table 1 {LS, LV, FM}, when inertia is finite (cf. figure 8). (Online version in colour.)

Figure 11 shows the power dissipation $\bar{P}(\bar{\omega})$ as a function of dimensionless frequency $\bar{\omega}$ for mode III, and for $De = 10^{-i}$, $i = \{1, 2, 3, 4\}$ and $De = 0$ (inset).

It is clear that inertia plays a crucial role in the amplitude and location of the power peak. At finite Deborah number ($De = 10^{-i}$; $\{i = 4, 3, 2, 1\}$), the system displays power peaks whose values are determined by the contrast of the viscoelastic phases, total bulk viscosity and membrane elastic ratio. The inset shows the inertialess case $De = 0$ with only a broad power plateau.

Figure 12 shows the power dissipation as a function of dimensionless frequency for $De = 10^{-4}$, $De = 0$ and for several membrane elasticity ratios. The material properties used in the simulation

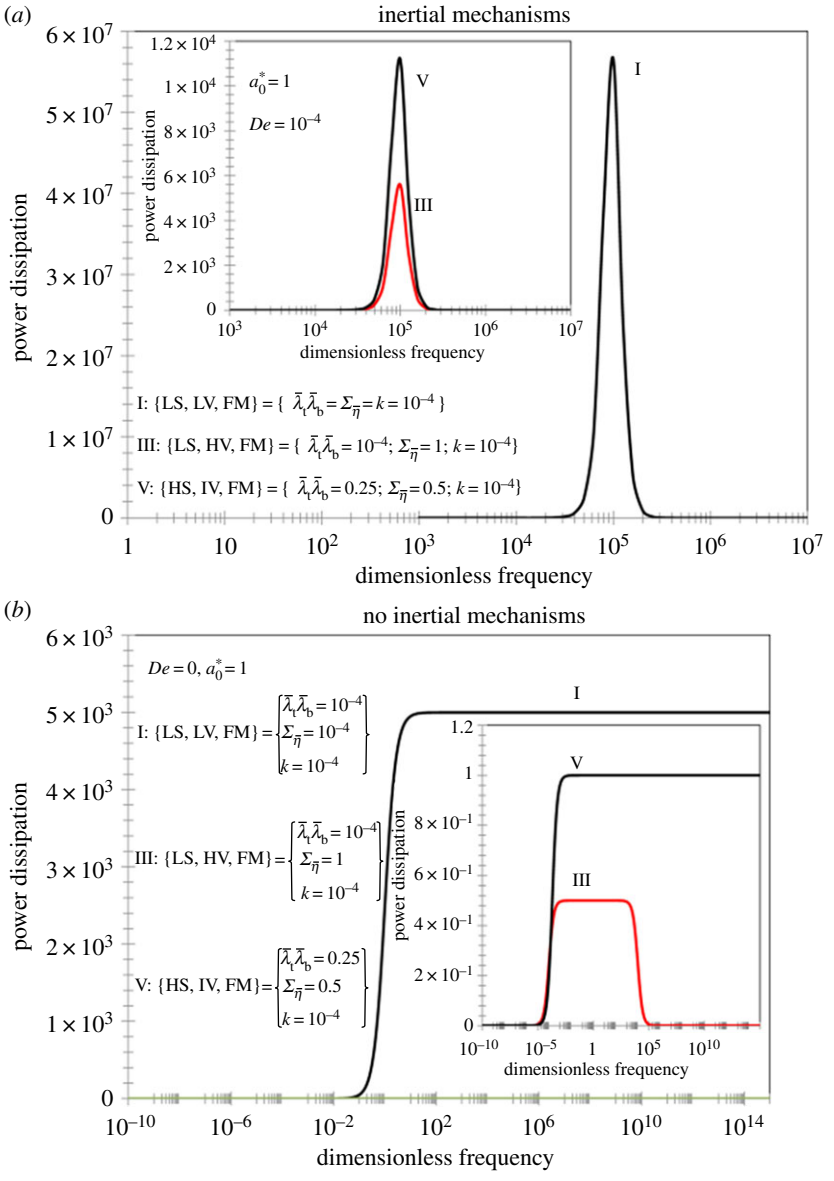

Figure 10. Power dissipation $\bar{P}(\bar{\omega})$ as a function of the dimensionless frequency $\bar{\omega}$ for the mode {I, III, V} in the cases where the inertial mechanisms are present (*a*) and absent (*b*). Inertia promotes the formation of localized power pulses. Intertialess conditions generate a wide plateau and only for mode III. (Online version in colour.)

correspond to mode III {LS, HV, FM}. It is clear that the elastic ratio k plays an important role in the amplitude, and affects the symmetry and frequency bandwidth of the resonance. As expected more floppy membranes will result in higher dissipation as they store more energy.

Figure 13 shows the elastic membrane energy as a function of dimensionless frequency under weak inertia for modes {I, III, IV}, for $De = 10^{-4}$ and $De = 0$. Inertia generates an asymmetric well, indicating storage and solid-like behaviour in the terminal and large frequency zones, as noted in equation (5.5). Inertialess conditions lead to an energy storage step, with little storage at large frequency since no solid behaviour exists at high frequency when $De = 0$. For brevity, we discuss only the key effects of fluid inertia (De) and membrane elasticity k on elastic storage (E). Increasing De decreases the width of the energy well and increasing k decreases its depth; the energy well is

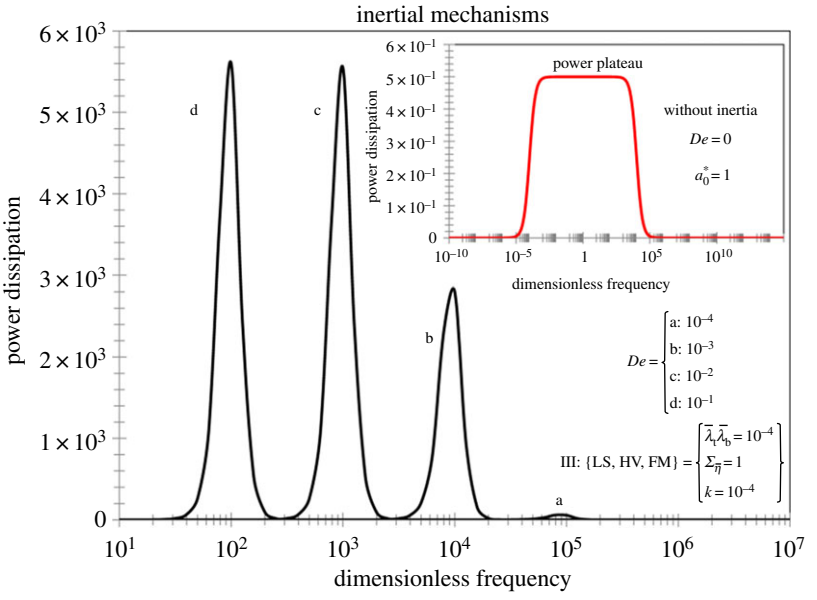

Figure 11. Power dissipation as a function of dimensionless frequency, for mode III (table 1) and increasing inertia (*De*). The material properties used in the simulation correspond to mode III {LS, HV, FM}. The inset shows the intertialess case ($De = 0$). Inertia generates well-localized narrow peaks. Absence of inertia generates at best (mode III) a broad plateau. (Online version in colour.)

shown in figure 13*a*. As noted above inertia introduces solid response in the terminal and large frequency zones because both the input and output have second time derivatives and hence increasing *De* narrows the well. Increasing k increases the role of membrane elasticity at any frequency and hence the well is shallower at larger k.

Figure 14 shows the Q-factor as a function of the dimensionless frequency for modes {I, III, V}. For figure 14*a* ($De = 10^{-4}$) the Q-factors are V-shaped with a superposed vertex blunting that increases with viscosity. Only modes I and III penetrate the important $Q(\bar{\omega}) < 1$ dissipation zone; small localized resonances are seen just prior to the increase of $Q(\bar{\omega})$. For figure 14*b* ($De = 0$), the Q-factors are J-shaped for mode I and III and blunted V-shaped for mode V. All modes penetrate into the important $Q(\bar{\omega}) < 1$ dissipation zone, but mode V renters the $Q(\bar{\omega}) > 1$ elastic zone at high frequency.

By combining the results from figures 8 to 14 and equations (4.9)–(4.11), we arrive at a qualitative picture of power delivery $\bar{P}(\bar{\omega})$ and of the $Q(\bar{\omega})$ factor of the device as a function of the elastic ratio k, presented in figure 15 in terms of the membrane stiffness. The region $k > 1/2$ is not relevant as the membrane is too stiff to absorb and release elastic energy. Since we demand $Q(\bar{\omega}) < 1$ and a power peak, only the lower left quadrant is relevant. Both conditions can be met only with mode I and $De \ll 1$, and with mode III and $De = 0$; all other modes and conditions do not fulfil these criteria. The key requirements are: (i) asymmetric fluid elasticity ($\bar{\lambda}_t\bar{\lambda}_b \ll 1$), (ii) membrane flexibility ($k < 1/2$), and (iii) either large viscosity and no inertia (III), or inertia and low viscosity (I).

The material parameters of importance are: (i) density of the two viscoelastic phases, (ii) elastic membrane stiffness, (iii) elasticity of the two viscoelastic phases, and (iv) Maxwell relaxation times. The specific ways to adapt these parameters are by changing the concentration and the molecular weight distribution of dissolved polymer chains. To increase power amplitude, one of the liquid phases must be weakly elastic and the other one completely viscoelastic (phase asymmetry). To shift the position of the localized power plateau and width of the power plateau, the elasticity of the membrane with respect to the bulk (viscoelastic phases) must be tuned.

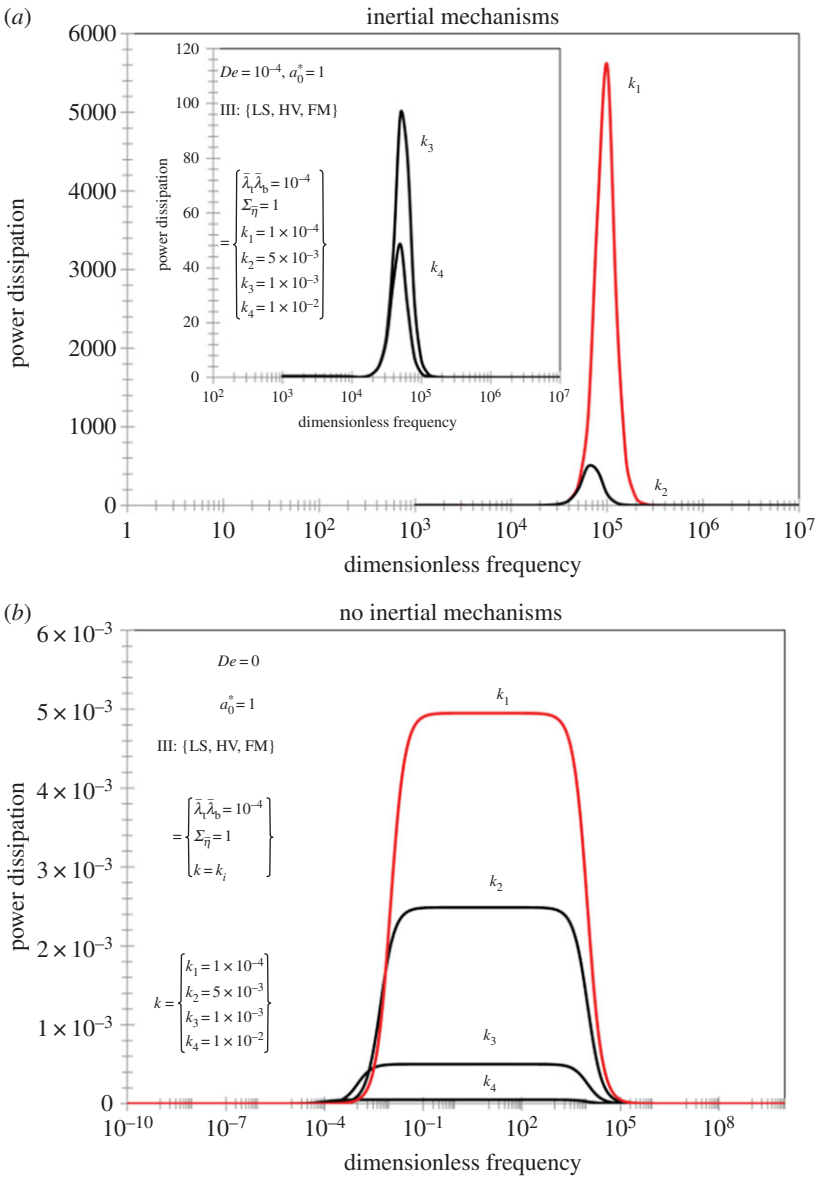

Figure 12. Power dissipation as a function of the dimensionless frequency for different values of the elastic ratio k and (*a*) $De = 10^{-4}$ and (*b*) $De = 0$. The material properties used in the simulation correspond to mode III. Softer membranes generate more power dissipation. (Online version in colour.)

To widen the power plateau, the Maxwell relaxation times, elasticity of the membrane and viscoelastic phases must be modified.

7. Conclusion

Membrane flexoelectricity is a novel electromechanical coupling effect that occurs in polarizable media under geometric curvature. The sensor effect is performed by bending induced electric polarization, whereas the converse actuation effect is performed by the membrane curvature induced by an imposed electric field. Membrane flexoelectricity is relevant to the biological functioning of the OHCs which act as amplifiers to counteract viscous dissipation through

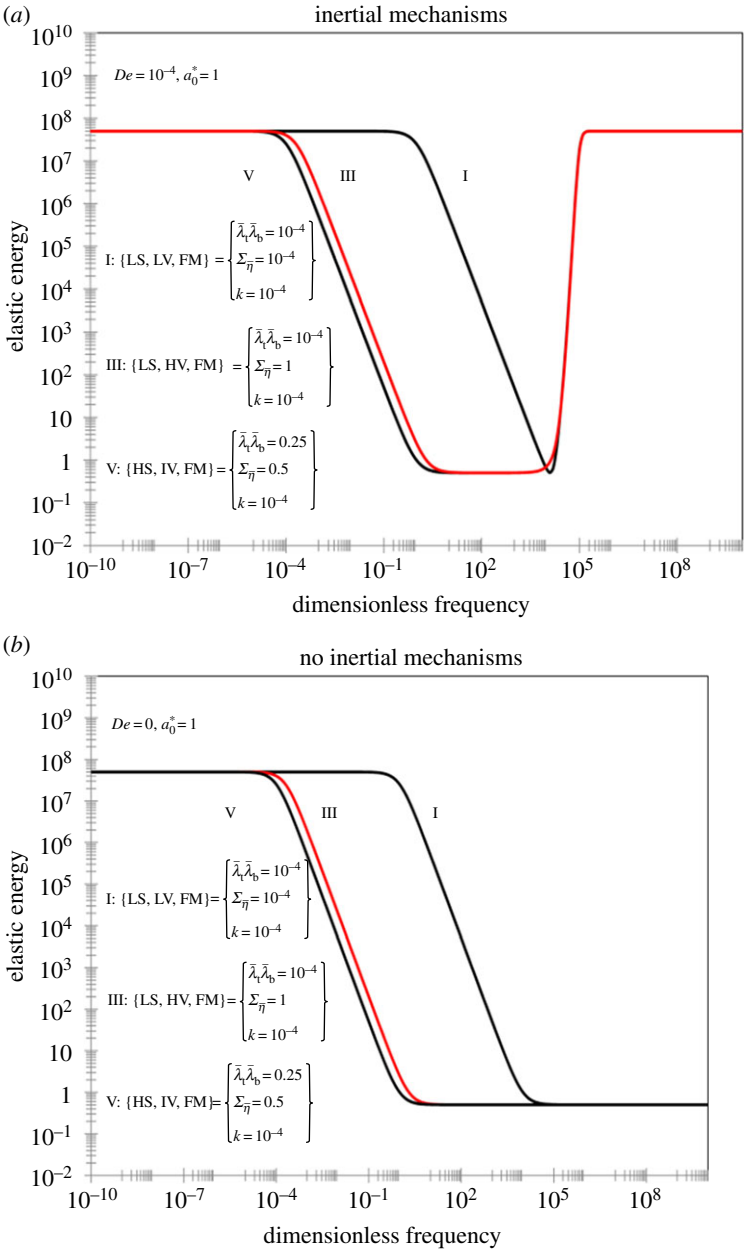

Figure 13. Elastic energy as a function of the dimensionless frequency for the three modes {I, III, V} for (*a*) $De = 10^{-4}$ and (*b*) $De = 0$. Inertia generates a well at intermediate frequencies. (Online version in colour.)

mechanic transduction and thus allowing hearing [11–13,20–28]. The key challenge is to understand the coupling of oscillatory flexoelectric actuation and the viscoelastic phenomena of the fluids that are in contact with the oscillating membrane [11–13]. An efficient method to describe membrane flexoelectricity is to use the LC analogy that follows by identifying the director field of a nematic with the unit normal to the membrane [11] (figure 2). A key parameter is the flexoelectric coefficient which for biological membranes is of the order of 3–20 pC m^{-1} [11]. In this paper, we explored the dynamics of the actuation flexoelectric mode taking into account the inertial mechanism. An integrated dynamical model for the average curvature of

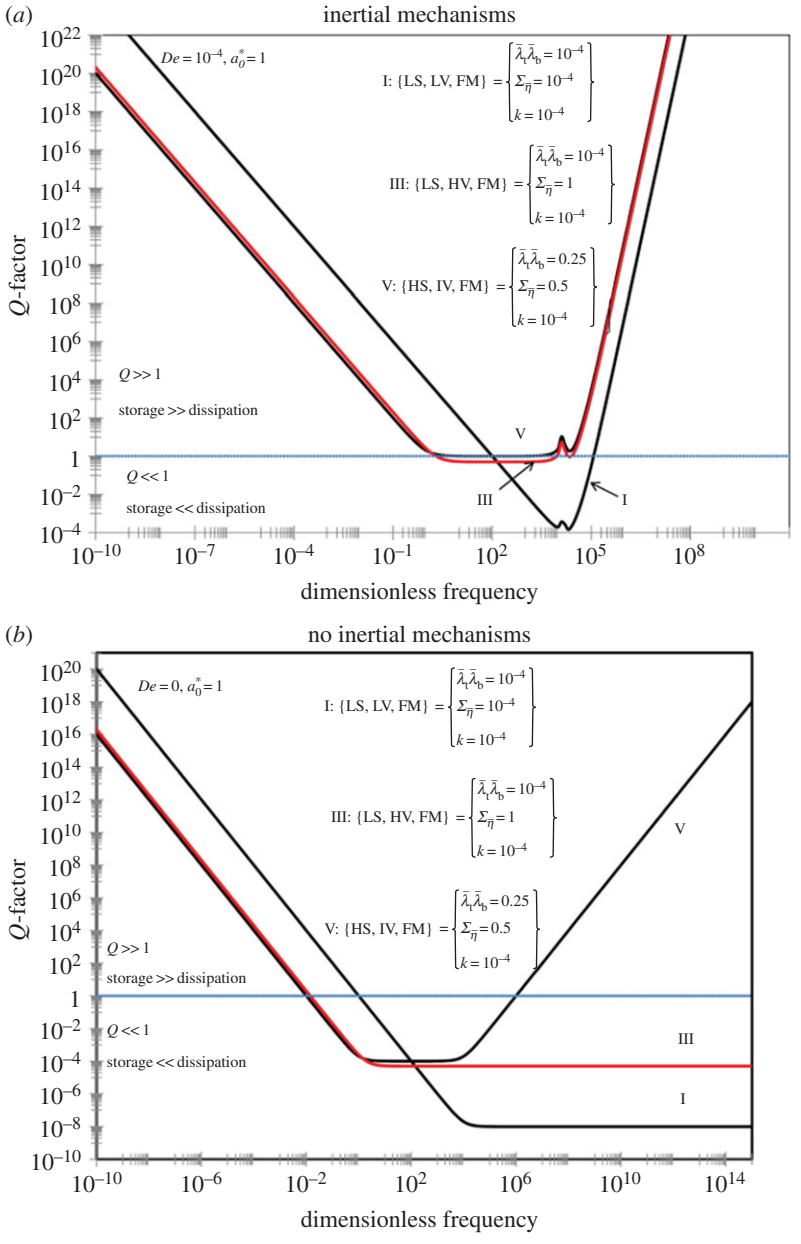

Figure 14. Q-factor as a function of the dimensionless frequencies for modes I, III, V, and (*a*) $De = 10^{-4}$ and (*b*) $De = 0$. The horizontal $Q(\bar{\omega}) = 1$ line divides the response in the regions of elastic or viscous dominated. (Online version in colour.)

flexoelectric membranes oscillating in viscoelastic fluid media under capillary confinement was formulated using a previously presented shape equation based on the LC approach [11–13]. The membrane curvature dynamics is given by a balance among the viscoelastic stress jump from the contacting bulk liquids, the restoring membrane effective tension, and the driving flexoelectric force (equations (2.1), (2.2), (2.5) and (2.9)) [11–13]. By using the flexoelectric shape equation in conjunction with a viscoelastic capillary flow model for the contacting phases (equation (2.8)), we obtained a new average curvature dynamic equation (equations (3.1) and (3.4)) [11]. By applying the Fourier transform to the governing partial linear differential equation (equation (3.1)) and using the relation between the speed of the average curvature

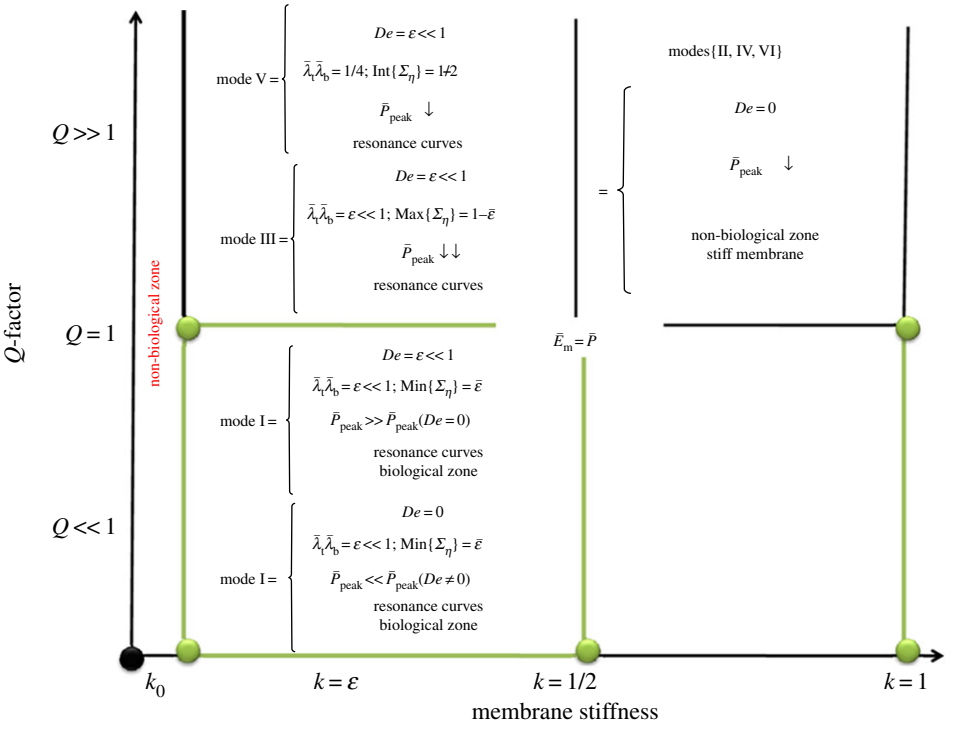

Figure 15. Device performance diagram in terms of Q-factor as a function of membrane elastic ratio k. The lower left quadrant represents performance conditions (power peak and $Q(\bar{\omega}) < 1$) relevant to biological flexoelectric membranes. (Online version in colour.)

and volumetric flow (equation (3.2)), a relationship between the average curvature and applied electrical field was found (equations (3.4) and (3.7)). The corresponding complex transfer function (equation (4.4)) is a function of the inertia, asymmetry of the viscoelastic phases, total bulk viscosity and membrane elasticity, through characteristic dimensionless numbers associated with each mechanisms (equations (3.5*a*,*b*) and (3.8*a*,*b*)). At small Deborah number, the complex transfer function reduces to a previous viscous model (equation (3.4)) studied at length in [11].

A thorough parametric study was performed to identify the conditions that lead to the emergence of a power pulse (table 1). It was found that the inertial mechanisms play an important role in the resonance curves associated with the power dissipation in the relevant modes {I, III, V}, which corresponds to the cases of low and high symmetries of the viscoelastic phases, low and sufficiently large total bulk viscosity and small elastic ratio indicating that less elasticity is stored in the membrane (table 2 and figures 8–10).

An evaluation of the present model predictions based on power profile indicates that the Helfrich–flexoelectric–Maxwell fluid model possesses the necessary physics to qualitatively capture electromechanical power conversion [11] (figures 9–14). The linear model presented here is valid only for electric fields of sufficiently small amplitude, high dimensionless frequencies and small deformations [11] (equations (3.1) and (4.4)).

The present theory, model and computations contribute to the evolving fundamental understanding of biological shape actuation through electromechanical couplings [5–9,11–13].

Funding statement. A.D.R. was supported by the US Office of Basic Energy Sciences, Department of Energy, grant no. DE-SC0001412. E.E.H.-V. gratefully acknowledges the financial fellowship support from CONACYT-MEXICO (postdoctoral grant no. 147870) and the Canadian Government through Foreign Affairs and International Trade Canada (DFAIT).

Conflict of interest. The authors declare no conflict of interest.

Appendix A

In order to non-dimensionalize equations (3.1)–(3.3), the following dimensionless variables are defined for the electrical field, curvature, time, frequency, viscoelastic properties and power:

$$\bar{E}=\frac{E}{E_0};\quad \bar{H}=aH;\quad \bar{r}=\frac{r}{a};\quad \bar{z}=\frac{z}{a};\quad \bar{t}=\frac{t}{\Sigma_\lambda};\quad \bar{\omega}=\Sigma_\lambda\omega;\quad \bar{G}_b=\frac{G_b}{\Sigma_G};\quad \bar{\lambda}_b=\frac{\lambda_b}{\Sigma_\lambda};$$
$$\bar{M}=\frac{M}{\Sigma_G};\quad \bar{Q}=\frac{Q}{\pi a^3/\Sigma_\lambda};\quad \bar{P}=\frac{P}{2\pi a^2 L\,(\Sigma_G/\Sigma_\lambda)};\quad \bar{E}m=\frac{Em}{2\pi a^2 L\Sigma_G}. \tag{A1)–(A10}$$

Notice that for equations (A 1)–(A 10), the following restrictions are satisfied: $\bar{X}_b+\bar{X}_t=1$; $X=\{G,\lambda\}$.

In equations (A 1)–(A 10), the characteristic macroscopic force, length, time, elastic force power and membrane elasticity are: (i) amplitude of the external electrical field, (ii) radius of the pipe, (iii) sum of the viscoelastic times in the bottom and the top fluids, and (iv) sum of the elastic moduli in the bottom and the top fluids . The energy (power) is scaled by the ratio between the sum of the elastic moduli and the viscoelastic time multiplied by characteristic axial and radial length scales (radius of the pipe and axial length). The selection of these characteristic times allows the comparison with the other internal (inertial, viscoelastic times) and external characteristic times (frequency).

Appendix B

The purpose of this appendix is to show the key derivation steps needed to perform a Fourier analysis of the model (equations (3.1) and (3.2)), derive the block diagram (figures 6 and 7), transfer functions (equations (4.5)–(4.8), (4.11) and (4.12)) and Kramers–Kroning relations (equations (4.9) and (4.10)).

(a) Flexoelectric momentum equation

The Fourier transform of $\{\bar{v}_z,\bar{p},\bar{E},\bar{H},\bar{Q}\}$ is

$$\bar{X}(\bar{r},\bar{\omega})=\frac{1}{\sqrt{2\pi}}\int_{-\infty}^{\infty}\mathrm{d}\bar{t}\mathrm{e}^{-j\bar{\omega}\bar{t}}\bar{x}(\bar{r},\bar{t});\bar{x}(\bar{r},\bar{t})=\{\bar{v}_z,\bar{p},\bar{E},\bar{H},\bar{Q}\}, \tag{B 1}$$

where $\mathrm{e}^{-\mathrm{i}\bar{\omega}\bar{t}}$ is the complex kernel. Applying the Fourier transform to the electro-rheological model given in equations (3.1) and (3.2) we get

$$\left\{(\Sigma_{\bar{\eta}}+\bar{\lambda}_t\bar{\lambda}_b(j\bar{\omega}))\frac{1}{\bar{r}}\frac{\partial}{\partial\bar{r}}\bar{r}\frac{\partial}{\partial\bar{r}}-De^2(1+(j\bar{\omega})+\bar{\lambda}_t\bar{\lambda}_b(j\bar{\omega})^2)(j\bar{\omega})\right\}\bar{v}_z(\bar{r},\bar{\omega})$$
$$=(1+(j\bar{\omega})+\bar{\lambda}_t\bar{\lambda}_b(j\bar{\omega})^2)4\left(a_0^*\bar{E}(\bar{\omega})-\left(\frac{k}{1-k}\right)\bar{H}(\bar{\omega})\right). \tag{B 2}$$

$$\int_0^1\bar{r}\bar{v}_z(\bar{r},\bar{\omega})\mathrm{d}\bar{r}=-\frac{1}{4}(j,\bar{\omega})\bar{H}(\bar{\omega}). \tag{B 3}$$

Equation (B 2) is a parametric Bessel differential equation. The general solution of (B 2) is the sum of the homogeneous and particular solutions:

$$\bar{v}z(\bar{r},\bar{\omega})=-\frac{4}{De^2(j\bar{\omega})}\left(1-\frac{J_0(\beta\bar{r})}{J_0(\beta)}\right)\left(a_0^*\bar{E}(\bar{\omega})-\left(\frac{k}{1-k}\right)\bar{H}(\bar{\omega})\right), \tag{B 4}$$

where $J_0(\beta\bar{r})$ are the first and second kind Bessel functions of order zero, respectively. In equation (B 4), we used the non-slip condition $\bar{v}_z(\bar{r}=1,\bar{\omega})=0$ and bounded the axial velocity in

all the domain, i.e. $|\bar{v}_z(\bar{r},\bar{\omega})| \le M$. The parameter $\beta^2 \in C$ is given by

$$\beta^2 = -De^2\varphi(\bar{\omega})\cdot(j\bar{\omega}) = -De^2\left(\frac{1+(j\bar{\omega})+\bar{\lambda}_t\bar{\lambda}_b(j\bar{\omega})^2}{\Sigma_{\bar{\eta}}+\bar{\lambda}_t\bar{\lambda}_b(j\bar{\omega})}\right)\cdot(j\bar{\omega}). \tag{B 5}$$

In equation (B 4), $\varphi(\bar{\omega}) \in C$ can be interpreted as a total complex fluidity of the two viscoelastic phases (inverse of the viscosity function, $\varphi(\bar{\omega}) \equiv \eta^{-1}(\bar{\omega})$). The volume flow rate in cylindrical coordinates can be calculated using the standard formula:

$$\Im(\bar{\xi}) = 2\int_0^1 \bar{v}_z(\bar{r},\bar{\omega})\bar{r}\,\mathrm{d}\bar{r} = -\frac{1}{8\bar{\Pi}(\bar{\omega},\beta))}\left(a_0^*\bar{E}(\bar{\omega}) - \left(\frac{k}{1-k}\right)\bar{H}(\bar{\omega})\right), \tag{B 6a}$$

where the generalized viscosity function is given by

$$\bar{\Pi}(\bar{\omega},\beta) = De^2(j\bar{\omega})\Big/64\left(1-2\frac{J_1(\beta)/\beta}{J_0(\beta)}\right). \tag{B 6b}$$

In equations (B 6), the property of the Bessel functions $\mathrm{d}[zJ_1(z)]/\mathrm{d}z = zJ_0(z)$ and the change of variable $z = \beta\bar{r}$ were used. In equation (B 6) the Bessel function of the first kind $J_1(\beta)$ was defined.

(b) Dynamic response

Equations (B 3) and (B 6) can be solved for the average membrane curvature, and by defining the ratio between the input (electrical field $\bar{E}(\bar{\omega})$) and output (curvature of the membrane), the transfer function is given by

$$F_D(\bar{\omega}) = \frac{\bar{H}(\bar{\omega})}{\bar{E}(\bar{\omega})} = F_S\frac{\{-(8/De^2\bar{\omega}^2)(1-2((J_1(\beta)/\beta)/J_0(\beta)))\}}{((1-k)/k)+\{-(8/De^2\bar{\omega}^2)(1-2((J_1(\beta)/\beta)/J_0(\beta)))\}} = F_S\frac{\mathrm{X}(\bar{\omega};\beta)}{((1-k)/k)+\mathrm{X}(\bar{\omega};\beta)}. \tag{B 7}$$

In equation (B 7), $F_S = a_0^*$ is the static transfer function. The complex function $\mathrm{X}(\bar{\omega};\beta)$ is defined as

$$\begin{aligned}\mathrm{X}(\bar{\omega};\beta) &= \frac{1}{De^2\bar{\omega}^2}\left(\beta^2+\frac{1}{6}\beta^4+\frac{11}{384}\beta^6+\frac{19}{3840}\beta^8+\frac{473}{552960}\beta^{10}+\mathrm{O}[\beta]^{11}\right)\\ &= \frac{1}{De^2\bar{\omega}^2}(\delta_1\beta^{2(1)}+\delta_2\beta^{2(2)}+\delta_3\beta^{2(3)}+\delta_4\beta^{2(4)}+\delta_5\beta^{2(5)}+\cdots+\delta_k\beta^{2(k)}).\end{aligned} \tag{B 8}$$

In equation (B 8), the power expansion of the Bessel functions was used. The coefficients $\{\delta_k\}_{k=1}^N$ are real negative numbers, i.e. $\{\delta_k\}_{k=1}^N \in R^+$ with $\delta_k < \delta_{k+1}$. Substituting the parameter $\beta^2 = -De^2(j\bar{\omega})\varphi(\bar{\omega})$ into equation (B 8), the transfer function in terms of an infinity power series is given by

$$F_D(\bar{\omega}) = F_S\frac{((1-k)/k)\sum_{k=1}^N \delta_k(De^2)^{k-1}\cdot(\bar{\omega})^{k-2}(j^3)^k(\varphi(\bar{\omega}))^k}{((1-k)/k)+\sum_{k=1}^N \delta_k(De^2)^{k-1}\cdot(\bar{\omega})^{k-2}(j^3)^k(\varphi(\bar{\omega}))^k}; \quad k\in N, \tag{B 9}$$

showing how De and the fluidity $\varphi(\bar{\omega})$ affect the response.

(c) Small Deborah numbers

At small values of the Deborah number, i.e. $De \ll 1$, the transfer function (equation (B 9)) can be developed up to the first term and using the fluidity function given by equation (B 5), the transfer function is given by:

$$\mathrm{Lim}_{De\to 0}F_D(\bar{\omega}) \approx F_S\frac{1-kb_2^*(k,\bar{\lambda}_t\bar{\lambda}_b)\bar{\omega}^2+j\bar{\omega}}{1-b_2^*(k,\bar{\lambda}_t\bar{\lambda}_b)\bar{\omega}^2+b_1^*(k,\Sigma_{\bar{\eta}})j\bar{\omega}} = \mathrm{Re}[F_D(\bar{\omega})]+j\mathrm{Im}[F_D(\bar{\omega})]. \tag{B 10}$$

Notice that equation (B 10) is the transfer function of equation (3.4). Taking the conjugate of the above expression we find

$$\mathrm{Re}[F_D(\bar{\omega})] = F_S\frac{1+(b_1^*(k,\Sigma_{\bar{\eta}})-(1+k)b_2^*(k,\bar{\lambda}_t\bar{\lambda}_b))\bar{\omega}^2+k(b_2^*(k,\bar{\lambda}_t\bar{\lambda}_b)\bar{\omega}^2)^2}{(1-b_2^*(k,\bar{\lambda}_t\bar{\lambda}_b)\bar{\omega}^2)^2+(b_1^*(k,\Sigma_{\bar{\eta}})\bar{\omega})^2} \tag{B 11}$$

and

$$\mathrm{Im}[F_{\mathrm{D}}(\bar{\omega})] = F_{\mathrm{S}} \frac{(1 - b_1^*(k, \Sigma_{\bar{\eta}}))\bar{\omega} + (1 - kb_1^*(k, \Sigma_{\bar{\eta}}))b_2^*\bar{\omega}^3}{(1 - b_2^*\bar{\omega}^2)^2 + (b_1^*\bar{\omega})^2}. \tag{B 12}$$

Equations (B 11) and (B 12) represent the real and imaginary parts of the transfer function $F_{\mathrm{D}}(\bar{\omega})$. Making the following identifications, we have:

$$H_{i0}(\bar{\omega}; \bar{\lambda}_{\mathrm{t}}\bar{\lambda}_{\mathrm{b}}, \Sigma_{\bar{\eta}}, k, a_0^*) = Re[F_{\mathrm{D}}(\bar{\omega})] \tag{B 13}$$

and

$$H_{0i}(\bar{\omega}; \bar{\lambda}_{\mathrm{t}}\bar{\lambda}_{\mathrm{b}}, \Sigma_{\bar{\eta}}, k, a_0^*) = |\mathrm{Im}[F_{\mathrm{D}}(\bar{\omega})]|. \tag{B 14}$$

Notice that the real and imaginary parts of the transfer function are the same as the average curvature moduli studied previously [18], and can be generalized for higher rheological linear models such as the well-known Jeffrey and Burgers models.

References

1. Rey AD. 2010 Liquid crystals models of biological materials and processes. *Soft Matter* **6**, 3402–3429. (doi:10.1039/B921576J)
2. Petrov AG. 2006 Electricity and mechanics of biomembrane systems: flexoelectricity in living membranes. *Anal. Chim. Acta* **568**, 70–83. (doi:10.1016/j.aca.2006.01.108)
3. Petrov AG. 2001 Flexoelectricity of model and living membranes. *Biochim. Biophys. Acta Biomembr*. **1561**, 1–25. (doi:10.1016/S0304-4157(01)00007-7)
4. Petrov AG. 1999 *The lyotropic state of matter: molecular physics and living matter physics*. Amsterdam, The Netherlands: Gordon and Breach.
5. Rey AD. 2006 Liquid crystals model of membrane flexoelectricity. *Phys. Rev. E* **74**, 011710. (doi:10.1103/PhysRevE.74.011710)
6. Rey AD. 2006 Polar fluid model of viscoelastic membranes and interfaces. *J. Colloid Interface Sci*. **304**, 226–238. (doi:10.1016/j.jcis.2006.08.027)
7. Rey AD. 2007 Capillary models for liquid crystal fibers, membranes, films, and drops. *Soft Matter* **2**, 1349–1368. (doi:10.1039/B704248P)
8. Rey AD. 2005 Mechanics of soft solid–liquid crystal interfaces. *Phys. Rev. E* **72**, 011706. (doi:10.1103/PhysRevE.72.011706)
9. Das S, Rey AD. 2006 Magnetic field-induced shape transitions in multiphase polymer-liquid crystal blends. *Macromol. Theory Simul*. **15**, 469–486. (doi:10.1002/mats.200600024)
10. Sachs F, Brownell WE, Petrov AG. 2009 Membrane electromechanics in biology, with a focus on hearing. *MRS Bull*. **34**, 665–670. (doi:10.1557/mrs2009.178)
11. Abou-Dakka M, Herrera-Valencia EE, Rey AD. 2012 Linear oscillatory dynamics of flexoelectric membranes embedded in viscoelastic media with applications to outer hair cells. *J. Non-Newtonian Fluid Mech*. **185–186**, 1–17. (doi:10.1016/j.jnnfm.2012.07.007)
12. Rey AD. 2008 Nonlinear actuator model for flexoelectric membranes. *Int. J. Design Nat. Ecodynam*. **3**, 28–38. (doi:10.2495/DNE-V3-N1-28-38)
13. Rey AD. 2008 Linear viscoelastic model for bending and torsional modes in fluid membranes. *Rheol. Acta* **47**, 861–871. (doi:10.1007/s00397-008-0259-2)
14. Rey AD, Servio P, Herrera-Valencia EE. 2013 Stress-sensor device based on flexoelectric liquid crystalline membranes. *ChemPhysChem* **15**, 1405–1412. (doi:10.1002/cphc.201300600)
15. Rey AD, Servio P, Herrera-Valencia EE. 2013 Bioinspired model of mechanical energy harvesting based on flexoelectric membranes. *Phys. Rev. E* **87**, 022505. (doi:10.1103/PhysRevE.87.022505)
16. Ehrenstein D, Iwasa KH. 1996 Viscoelastic relaxation in the membrane of the auditory outer hair cell. *Biophys. J*. **71**, 1087–1094. (doi:10.1016/S0006-3495(96)79310-4)
17. Rey AD, Herrera-Valencia EE, Kumar Murugesan Y. 2013 Structure and dynamics of biological liquid crystals. *Liq. Cryst*. **41**, 430–451. (doi:10.1080/02678292.2013.845698)
18. Rey AD, Herrera-Valencia EE. 2012 Liquid crystal models of biological materials and silk spinning. *Biopolymers* **97**, 374–396. (doi:10.1002/bip.21723)
19. Rey AD, Herrera-Valencia EE. 2012 Rheological theory and simulations of surfactant nematic liquid crystals. In *Self-assembled supramolecular architectures: lyotropic liquid crystals* (eds N Garti, P Somasundaran, R Mezzenga), pp. 21–68. Hoboken, NJ: John Wiley & Sons Inc.

20. Messini N, Karabarbounis A, Philippetis AL, Margaritis LH. 2002 Mechanism for action of electromagnetic field on cells. *Biochem. Biophys. Res. Commun*. **298**, 95–102. (doi:10.1016/S0006-291X(02)02393-8)
21. Oghalai JS, Zhao HB, Kutz JW, Brownell WE. 2000 Voltage- and tension-dependent lipid mobility in the outer hair cell plasma membranes. *Science* **287**, 658–661. (doi.10.1126/science.287.5453.658)
22. Brownell WE. 1985 Evoked mechanical responses of isolated cochlear outer hair cells. *Science* **227**, 194–196. (doi:10.1126/science.3966153)
23. Rabbits RD, Clifford S, Breneman KD, Farrell B, Brownell WE. 2009 Power efficiency of outer hair cell somatic electromotility. *PLoS Comput. Biol*. **5**, e1000444. (doi:10.1371/journal.pcbi.1000444)
24. Spector AA, Deo N, Ratnanather JT, Raphael RM. 2006 Electromechanical models of the outer hair cell composite membrane. *J. Membr. Biol*. **209**, 135–152. (doi:10.1007/s00232-005-0843-7)
25. Raphael RM, Popel AS, Brownell WE. 2000 A membrane bending model of outer hair cell electromotility. *Biophys. J*. **78**, 2844–2862. (doi:10.1016/S0006-3495(00)76827-5)
26. Hawkins RD, Lovett M. 2004 The developmental genetics of auditory hair cells. *Hum. Mol. Genet*. **13**, R289–R296. (doi:10.1093/hmg/ddh249)
27. Sachs F, Brownell WE, Petrov AG. 2009 Membrane electromechanics in biology, with a focus on hearing. *MRS Bull*. **34**, 665–670. (doi:10.1557/mrs2009.178)
28. Fikus M, Pawlowski P. 1989 Bioelectrorheolgical model of the cell. 2. Analysis of creep and its experimental verification. *J. Theor. Biol*. **137**, 365–373. (doi:10.1016/S0022-5193(89)80035-9)
29. Walas SM. 1991 *Modeling with differential equations in chemical engineering*. Butterworth-Heinemann Series in Chemical Engineering. Boston, MA: Butterworth-Heinemann.